

An energy-decreasing algorithm for the finite element approximation of ferronematic equilibrium states

Alexandre Ern[‡] Ruma R. Maity[§]

May 13, 2026

Abstract

We develop an energy-decreasing algorithm for the finite element approximation of two-dimensional ferronematic equilibrium states. The problem is formulated as the minimization of the harmonic energy of two two-dimensional vector fields, both with prescribed length, together with an additional nonlinear relation on the orientation of the two vectors. The finite element setting is based on piecewise continuous finite elements on a weakly acute triangulation. The computational realization of the energy-decreasing algorithm employs a decomposition-coordination framework and a Uzawa-like iteration. Numerical experiments are presented to illustrate the computational performances of the algorithm.

Keywords: Liquid crystals, ferronematics, harmonic map, finite element method, energy-decreasing iterations, decomposition-coordination method

Mathematics Subject Classification. 65N30, 49M27, 76A15, 58E20

1 Introduction

Nematic liquid crystals are a physical state of a material where the constituent molecules exhibit long-range orientational ordering but no long-range positional ordering [15]. The study of composite systems consisting of magnetic nanoparticles dispersed in a nematic liquid crystal is commonly referred to as ferronematics in the literature [12, 21]. The nemato-magnetic coupling enhances magnetic susceptibility, enabling low-field control of material behavior with potential applications in optics, sensors, and telecommunications [18, 24]. Ferronematic equilibrium states are sought as minimizers of a suitable free energy density of the system, which generally consists of the Landau–de Gennes free energy density for the nematic liquid crystal, plus the Ginzburg–Landau free energy density for the magnetization, and the nemato-magnetic coupling energy density (see, e.g., [9] and the references cited therein). We focus here on a two-dimensional setting, where the ferronematic system occupies an open, bounded, connected, Lipschitz set (domain) $\Omega \subset \mathbb{R}^2$. In this case, the two variables describing the state of the system are: (i) The nematic liquid crystal tensor, \mathbf{Q} , a mapping from Ω to the space of symmetric, trace-free matrices in $\mathbb{R}^{2 \times 2}$; this is the so-called order parameter that describes the orientational ordering; (ii) The magnetization vector, \mathbf{M} , a mapping from Ω to \mathbb{R}^2 , represents the spatially averaged magnetic moment of the suspended nanoparticles. Owing to the two-dimensional setting, the order parameter \mathbf{Q} can be viewed as a vector in \mathbb{R}^2 as well. Altogether, the dependent variables are collected in the \mathbb{R}^4 -valued vector $\Psi := (\mathbf{Q}, \mathbf{M})^\top$.

We are particularly interested in the practically important case where the ratio (ℓ) between the material-dependent length scale and the computational domain length scale takes very small values. In this situation, equilibrium states can still be explored numerically using the above free energy density, but

[‡]CERMICS, CNRS, ENPC, Institut Polytechnique de Paris, 6 & 8 avenue B. Pascal, 77455 Marne-la-Vallée, France, and Inria, 48 Rue Barrault, 75647 Paris, France. Email: alexandre.ern@enpc.fr.

[§]Department of Mathematics, Indian Institute of Science, Bangalore, 560012, India and Engineering Mathematics, University of Innsbruck, 6020 Innsbruck, Austria. Email: rumaranim@iisc.ac.in.

this becomes particularly demanding computationally as the Euler–Lagrange minimization conditions lead to a system of four coupled nonlinear PDEs. Examples can be found in [9, 14, 20]. An alternative approach is to formally let the parameter ℓ approach zero and tackle directly the free energy density minimization under the additional constraint resulting from the above limit. Specifically, one enforces length constraints on the two-dimensional vectors \mathbf{Q} and \mathbf{M} , and a nonlinear relation expressing \mathbf{Q} in terms of \mathbf{M} . Altogether, this means that the values of Ψ are prescribed to lie in \mathcal{N} , a connected, compact, one-dimensional smooth submanifold of \mathbb{R}^4 . This is the approach followed herein, where nematic equilibrium states in the above asymptotic limit are modeled by minimizing the harmonic energy functional $E : H^1(\Omega; \mathbb{R}^4) \rightarrow \mathbb{R}$ such that (see Section 2 for more details on the notation)

$$E(\Psi) := \frac{1}{2} \int_{\Omega} \|\nabla \Psi\|_{\mathbb{R}^{4 \times 2}}^2 dx = \frac{1}{2} \int_{\Omega} \|\nabla \mathbf{Q}\|_{\mathbb{R}^{2 \times 2}}^2 dx + \frac{1}{2} \int_{\Omega} \|\nabla \mathbf{M}\|_{\mathbb{R}^{2 \times 2}}^2 dx, \quad (1.1)$$

subjected to the constraint that Ψ takes values in \mathcal{N} . Moreover, boundary values are prescribed on $\partial\Omega$ that are compatible with the above constraint. We assume the existence of a minimizer. Sufficient conditions for the Ginzburg–Landau problem are discussed in [8] based on the notion of winding numbers for the Dirichlet boundary datum.

The main goal of the paper is to analyze the finite element approximation of the above constrained minimization problem of the harmonic energy and to propose an energy-decreasing iterative algorithm with reasonable computational costs. We consider piecewise affine, continuous finite elements on a weakly acute triangulation \mathcal{T} [11, 16, 25]. Weakly acute triangulations are commonly used in the context of finite element approximations of harmonic energy minimization under length constraints. In the present setting, this assumption allows us to write the discrete harmonic energy as a sum of local positive contributions indexed by pairs of mesh nodes sharing a mesh edge. Furthermore, the constraint of taking values in \mathcal{N} is enforced at the mesh nodes. Incidentally, this means that we are considering a nonconforming approximation as the discrete functions $\Psi_{\mathcal{T}} : \Omega \rightarrow \mathbb{R}^4$ do not take values in \mathcal{N} everywhere in Ω (but only at the mesh nodes).

We first study how to devise energy-decreasing iterations at the continuous level. To this purpose, we leverage a representation of every element in the constraint manifold \mathcal{N} by a unit vector \mathbf{n} from the unit circle \mathcal{S} in \mathbb{R}^2 . The key relation to ensure the energy-decreasing property is the identity (2.8) below, relating the (spatial) gradient of Ψ to the (spatial) gradient of \mathbf{n} . Unfortunately, it is not possible to extend this result to the discrete level. The first key idea forward, exploiting the weakly acute property of the mesh, is to replace the identity (2.8) at the continuous level by the identity (3.6), which evaluates the harmonic energy of a discrete field $\Psi_{\mathcal{T}}$ by a finite sum of positive contributions resulting from local increments of unit vectors associated with pairs of mesh nodes sharing a mesh edge. However, two unit vectors per mesh node need to be considered (and not just one), the two being related by a nonlinear mapping from \mathcal{S} onto itself. The second key idea forward is achieved by Lemma 3.2 which uncovers a subtle geometric property of the constraint manifold \mathcal{N} . The result of Lemma 3.2 brings the central design condition that guarantees the energy-decreasing property of the present iterative algorithm.

To enhance the computational efficiency of the energy-decreasing iterative algorithm, we adopt a decomposition-coordination approach in the spirit of Fortin and Glowinski’s framework for constrained optimization with separable objective functions and coupled constraints [17]. The constraint is incorporated using a Lagrange multiplier within an augmented Lagrangian approach [6, 7]. A critical point of the augmented Lagrangian is sought using an Uzawa-type iterative algorithm [2, 17]. As the primal minimization problem remains nonlinear, a further simplification is introduced by linearizing the constraint at each step of the Uzawa algorithm.

The minimization of the harmonic energy under prescribed length constraints is already well explored in the literature. The simplest setting is the Oseen–Frank model which minimizes the harmonic energy of a unit direction vector [1, 13, 19], see also [23] for further computational enhancements, [3] for the stability and convergence analysis and [4] for the implicit time discretization of harmonic map flows into spheres. More complex models have been addressed as well, including the Eriksen model where the dependent variable is the tensor $\mathbf{Q} = s(\mathbf{n} \otimes \mathbf{n} - d^{-1}\mathbb{I})$, where the order parameters are the scalar-valued function s and the field \mathbf{n} taking values in the unit sphere of \mathbb{R}^d , and d is the ambient space dimension

[5, 10, 22]. However, to the best of the authors' knowledge, numerical methods addressing the present ferronematic equilibrium problem have not yet been analyzed.

The remainder of this paper is organized as follows. Section 2 introduces the admissible constraint manifold \mathcal{N} and formulates the energy minimization problem. This section also outlines the continuous energy-decreasing algorithm. The main result of this section is Theorem 2.4. Section 3 develops the finite element approximation, leading to the discrete energy-decreasing algorithm. The main results of this section are Lemma 3.2 and Theorem 3.3. Section 4 describes important computational aspects, including the decomposition-coordination approach and the Uzawa-like iterations. Finally, Section 5 reports numerical experiments on two examples featuring nonzero smooth Dirichlet boundary conditions on a square domain, thereby illustrating the computational performance of the proposed algorithms.

2 Continuous setting

For positive integer numbers p, q , $\|\bullet\|_{\mathbb{R}^q}$ denotes the Euclidean norm in \mathbb{R}^q and $\|\bullet\|_{\mathbb{R}^{p \times q}}$ denotes the Frobenius norm in $\mathbb{R}^{p \times q}$. The Cartesian components of a vector $\Psi \in \mathbb{R}^q$ are denoted $(\Psi_i)_{1 \leq i \leq q}$.

2.1 Admissible manifold

Let \mathcal{S} be the unit sphere (circle) in \mathbb{R}^2 , $\mathbf{e}_1 := (1, 0)^\top$ the first vector of the Cartesian basis of \mathbb{R}^2 , and \mathbb{I} the 2×2 identity matrix. We consider the (nonlinear) map

$$\mathbf{R} : \mathcal{S} \rightarrow \mathcal{S}, \quad \mathbf{n} \mapsto \mathbf{R}(\mathbf{n}) := (2\mathbf{n} \otimes \mathbf{n} - \mathbb{I})\mathbf{e}_1. \quad (2.1)$$

An elementary computation shows that, if $\mathbf{n} \in \mathcal{S}$ is parametrized as $\mathbf{n} := (\cos(\varphi), \sin(\varphi))^\top$, then $\mathbf{R}(\mathbf{n}) = (\cos(2\varphi), \sin(2\varphi))^\top$. Given two positive real numbers Q_c and M_c , we define the (nonlinear) map

$$\mathcal{G} : \mathcal{S} \rightarrow \mathbb{R}^4, \quad \mathbf{n} \mapsto \mathcal{G}(\mathbf{n}) := (Q_c \mathbf{R}(\mathbf{n}), M_c \mathbf{n})^\top. \quad (2.2)$$

It is readily seen that $\mathcal{G} : \mathcal{S} \rightarrow \mathcal{N}$ is a smooth diffeomorphism, where

$$\mathcal{N} := \{\mathcal{G}(\mathbf{n}) \mid \mathbf{n} \in \mathcal{S}\} \subset \mathbb{R}^4. \quad (2.3)$$

We observe that \mathcal{N} is a connected, compact, one-dimensional smooth submanifold of \mathbb{R}^4 . For all $\mathbf{n} \in \mathcal{S}$, let $T_{\mathbf{n}}\mathcal{S}$ denote the tangent space of \mathcal{S} at \mathbf{n} , i.e., $T_{\mathbf{n}}\mathcal{S} = \{\mathbf{v} \in \mathbb{R}^2 \mid \mathbf{v} \cdot \mathbf{n} = 0\}$. Similarly, let $T_{\mathcal{G}(\mathbf{n})}\mathcal{N}$ denote the tangent space of \mathcal{N} at $\mathcal{G}(\mathbf{n})$. The differential of \mathcal{G} at $\mathbf{n} \in \mathcal{S}$, $d\mathcal{G}(\mathbf{n}) : T_{\mathbf{n}}\mathcal{S} \rightarrow T_{\mathcal{G}(\mathbf{n})}\mathcal{N}$ is given by, for all $\mathbf{n} = (n_1, n_2)^\top \in \mathcal{S}$ and all $\mathbf{v} = (v_1, v_2)^\top \in T_{\mathbf{n}}\mathcal{S}$,

$$\langle d\mathcal{G}(\mathbf{n}), \mathbf{v} \rangle = \begin{pmatrix} 2Q_c(v_1\mathbf{n} + n_1\mathbf{v}) \\ M_c\mathbf{v} \end{pmatrix} = \begin{pmatrix} 4Q_cn_1v_1 \\ 2Q_c(n_1v_2 + n_2v_1) \\ M_cv_1 \\ M_cv_2 \end{pmatrix}. \quad (2.4)$$

Lemma 2.1 (Norm). *We have $\|\langle d\mathcal{G}(\mathbf{n}), \mathbf{v} \rangle\|_{\mathbb{R}^4}^2 = (4Q_c^2 + M_c^2)\|\mathbf{v}\|_{\mathbb{R}^2}^2$.*

Proof. Since $v_1n_1 + v_2n_2 = 0$, the first component of $\langle d\mathcal{G}(\mathbf{n}), \mathbf{v} \rangle$ rewrites $2Q_c(n_1v_1 - n_2v_2)$. Since $(n_1v_1 - n_2v_2)^2 + (n_1v_2 + n_2v_1)^2 = (n_1^2 + n_2^2)(v_1^2 + v_2^2) = \|\mathbf{n}\|_{\mathbb{R}^2}^2\|\mathbf{v}\|_{\mathbb{R}^2}^2 = \|\mathbf{v}\|_{\mathbb{R}^2}^2$, the conclusion is straightforward. \square

2.2 Minimization problem

Let Ω be an open, bounded, connected, Lipschitz set (domain) in \mathbb{R}^2 . Given some Dirichlet boundary data $\Psi^b \in H^{\frac{1}{2}}(\partial\Omega; \mathbb{R}^4)$ taking values in \mathcal{N} a.e. in $\partial\Omega$, we consider the functional space

$$\mathcal{W} := \{\Phi \in H^1(\Omega; \mathbb{R}^4) \mid \Phi(\mathbf{x}) \in \mathcal{N} \text{ a.e. } \mathbf{x} \in \Omega \wedge \Phi|_{\partial\Omega} = \Psi^b\}, \quad (2.5)$$

and the (Dirichlet) energy functional

$$E : H^1(\Omega; \mathbb{R}^4) \rightarrow \mathbb{R}, \quad \Phi \mapsto E(\Phi) := \frac{1}{2} \int_{\Omega} \|\nabla \Phi\|_{\mathbb{R}^{4 \times 2}}^2 dx. \quad (2.6)$$

We assume that there exists $\Psi^* \in W$. Sufficient conditions for the Ginzburg–Landau problem are discussed in [8] based on the notion of winding numbers for Ψ^b .

Our goal is to solve the following constrained minimization problem:

$$\min_{\Phi \in W} E(\Phi). \quad (2.7)$$

As E is strongly convex and W is a nonempty, closed (but nonconvex) set, the model problem (2.7) admits at least one solution in W .

Lemma 2.2 (Composition using \mathcal{G}). (i) Let $\mathbf{n} \in H^1(\Omega; \mathbb{R}^2)$ take values in \mathcal{S} a.e. in Ω ; then $\Psi := \mathcal{G} \circ \mathbf{n} \in H^1(\Omega; \mathbb{R}^4)$ and takes values in \mathcal{N} a.e. in Ω . (ii) Let $\Psi \in H^1(\Omega; \mathbb{R}^4)$ take values in \mathcal{N} a.e. in Ω ; then, $\mathbf{n} := \mathcal{G}^{-1} \circ \Psi \in H^1(\Omega; \mathbb{R}^2)$ and takes values in \mathcal{S} a.e. in Ω .

Proof. (1) Proof of (i). By construction, Ψ takes values in \mathcal{N} a.e. in Ω . Since \mathcal{G} is bounded and Ω is a bounded set, $\Psi \in L^2(\Omega; \mathbb{R}^4)$. Letting ∂_k denote the partial derivative in the k -th Cartesian direction, for all $k \in \{1, 2\}$, we observe that

$$\partial_k \Psi = \langle d\mathcal{G}(\mathbf{n}), \partial_k \mathbf{n} \rangle.$$

Owing to Lemma 2.1, we infer that

$$\|\partial_k \Psi\|_{\mathbb{R}^4}^2 = (4Q_c^2 + M_c^2) \|\partial_k \mathbf{n}\|_{\mathbb{R}^2}^2 \quad \forall k \in \{1, 2\}. \quad (2.8)$$

Since $\mathbf{n} \in H^1(\Omega; \mathbb{R}^2)$ by assumption, this shows that $\Psi \in H^1(\Omega; \mathbb{R}^4)$.

(2) Proof of (ii). The proof is straightforward since $\mathbf{n} := \mathcal{G}^{-1} \circ \Psi = M_c^{-1}(\Psi_3, \Psi_4)^T$. \square

2.3 Energy-decreasing algorithm

Before presenting the algorithm, we recall some elementary properties of the projection $P_{\mathcal{S}}$ from $\mathbb{R}_*^2 := \mathbb{R}^2 \setminus \{\mathbf{0}\}$ onto \mathcal{S} , i.e., $P_{\mathcal{S}}(\mathbf{x}) := \frac{1}{\|\mathbf{x}\|_{\mathbb{R}^2}} \mathbf{x}$ for all $\mathbf{x} \in \mathbb{R}_*^2$. Set

$$\mathbb{R}_{\geq 1}^2 := \{\mathbf{x} \in \mathbb{R}^2 \mid \|\mathbf{x}\|_{\mathbb{R}^2} \geq 1\}. \quad (2.9)$$

Lemma 2.3 (Projection onto sphere). (i) $\|P_{\mathcal{S}}(\mathbf{x}) - P_{\mathcal{S}}(\mathbf{y})\|_{\mathbb{R}^2} \leq \|\mathbf{x} - \mathbf{y}\|_{\mathbb{R}^2}$ for all $\mathbf{x}, \mathbf{y} \in \mathbb{R}_{\geq 1}^2$. (ii) For all $\mathbf{v} \in H^1(\Omega; \mathbb{R}^2)$ taking values in $\mathbb{R}_{\geq 1}^2$, $P_{\mathcal{S}}(\mathbf{v}) \in H^1(\Omega; \mathbb{R}^2)$ and takes values in \mathcal{S} ; moreover, $\|\nabla P_{\mathcal{S}}(\mathbf{v})\|_{\mathbb{R}^{2 \times 2}} \leq \|\nabla \mathbf{v}\|_{\mathbb{R}^{2 \times 2}}$.

Proof. The statement (i) is just a consequence of the fact that, when acting on $\mathbb{R}_{\geq 1}^2$, $P_{\mathcal{S}}$ is the projection onto \mathcal{B}^1 , the unit ball of \mathbb{R}^2 which is a closed convex set. The statement (ii) follows from the same arguments, see also [1, Prop. 1]. \square

Given an initial guess $\Psi^0 \in W$, our goal is to generate a sequence $(\Psi^j)_{j=1}^{\infty}$ in W that is energy-decreasing, i.e.,

$$E(\Psi^{j+1}) \leq E(\Psi^j), \quad \forall j \geq 0. \quad (2.10)$$

At iteration $j \geq 0$, given $\Psi^j \in W$, the algorithm proceeds in four steps:

1. Set $\mathbf{n}^j := \mathcal{G}^{-1} \circ \Psi^j$. Owing to Lemma 2.2(ii), $\mathbf{n}^j \in H^1(\Omega; \mathbb{R}^2)$ and takes values in \mathcal{S} a.e. in Ω .

2. Define the linear space $\mathbf{K}^j := \{\mathbf{w} \in H_0^1(\Omega; \mathbb{R}^2) \mid \mathbf{w}(\mathbf{x}) \in T_{n^j(\mathbf{x})}\mathcal{S} \text{ a.e. } \mathbf{x} \in \Omega\}$ and solve the constrained minimization problem

$$\mathbf{w}^j := \arg \min_{\mathbf{w} \in \mathbf{K}^j} \frac{1}{2} \int_{\Omega} \|\nabla(\mathbf{n}^j - \mathbf{w})\|_{\mathbb{R}^{2 \times 2}}^2 dx. \quad (2.11)$$

This is a well-posed problem since the functional is strongly convex in $H_0^1(\Omega; \mathbb{R}^2)$ and the minimizing set is a closed convex subset of $H_0^1(\Omega; \mathbb{R}^2)$. Moreover, since $\mathbf{w}^j(\mathbf{x}) \cdot \mathbf{n}^j(\mathbf{x}) = 0$ and $\|\mathbf{n}^j(\mathbf{x})\|_{\mathbb{R}^2} = 1$ a.e. in Ω , we infer that $\mathbf{n}^j - \mathbf{w}^j$ takes values in $\mathbb{R}_{\geq 1}^2$ a.e. in Ω (observe that $\|\mathbf{n}^j(\mathbf{x}) - \mathbf{w}^j(\mathbf{x})\|_{\mathbb{R}^2}^2 = 1 + \|\mathbf{w}^j(\mathbf{x})\|_{\mathbb{R}^2}^2 \geq 1$).

3. Set $\mathbf{n}^{j+1} := P_{\mathcal{S}} \circ (\mathbf{n}^j - \mathbf{w}^j)$. Owing to Lemma 2.3, $\mathbf{n}^{j+1} \in H^1(\Omega; \mathbb{R}^2)$ and takes values in \mathcal{S} .
4. Set $\Psi^{j+1} := \mathcal{G} \circ \mathbf{n}^{j+1}$. Owing to Lemma 2.2(i), $\Psi^{j+1} \in H^1(\Omega; \mathbb{R}^4)$ and takes values in \mathcal{N} a.e. in Ω . Moreover, for a.e. $\mathbf{x} \in \partial\Omega$, we have $\mathbf{w}^j(\mathbf{x}) = \mathbf{0}$ so that $\mathbf{n}^{j+1}(\mathbf{x}) = P_{\mathcal{S}}(\mathbf{n}^j(\mathbf{x})) = \mathbf{n}^j(\mathbf{x})$; hence, $\Psi^{j+1}(\mathbf{x}) = \mathcal{G}(\mathcal{G}^{-1}(\Psi^j(\mathbf{x}))) = \Psi^j(\mathbf{x}) = \Psi^b(\mathbf{x})$. In conclusion, we have $\Psi^{j+1} \in W$ as claimed.

Theorem 2.4 (Energy decay). *The sequence $(\Psi^j)_{j=1}^{\infty}$ satisfies (2.10).*

Proof. Owing to (2.8), we infer that

$$\|\nabla \Psi^m\|_{\mathbb{R}^{4 \times 2}}^2 = (4Q_c^2 + M_c^2) \|\nabla \mathbf{n}^m\|_{\mathbb{R}^{2 \times 2}}^2 \quad \forall m \in \{j, j+1\}.$$

Moreover, owing to Lemma 2.3(ii), we infer that

$$\int_{\Omega} \|\nabla \mathbf{n}^{j+1}\|_{\mathbb{R}^{2 \times 2}}^2 dx \leq \int_{\Omega} \|\nabla(\mathbf{n}^j - \mathbf{w}^j)\|_{\mathbb{R}^{2 \times 2}}^2 dx \leq \int_{\Omega} \|\nabla \mathbf{n}^j\|_{\mathbb{R}^{2 \times 2}}^2 dx,$$

where the second bound follows from (2.11) and the observation that $\mathbf{0} \in \mathbf{K}^j$. Putting everything together gives

$$\begin{aligned} \int_{\Omega} \|\nabla \Psi^{j+1}\|_{\mathbb{R}^{4 \times 2}}^2 dx &= (4Q_c^2 + M_c^2) \|\nabla \mathbf{n}^{j+1}\|_{\mathbb{R}^{2 \times 2}}^2 \\ &\leq (4Q_c^2 + M_c^2) \int_{\Omega} \|\nabla \mathbf{n}^j\|_{\mathbb{R}^{2 \times 2}}^2 dx = \int_{\Omega} \|\nabla \Psi^j\|_{\mathbb{R}^{4 \times 2}}^2 dx. \end{aligned}$$

This completes the proof. \square

3 Finite element approximation

3.1 Discrete setting

We assume that Ω is a polygonal domain in \mathbb{R}^2 and consider a triangulation \mathcal{T} that covers Ω exactly. The collection of mesh vertices is partitioned as $\mathcal{V}_{\mathcal{T}} := \mathcal{V}_{\mathcal{T}}^{\circ} \cup \mathcal{V}_{\mathcal{T}}^{\partial}$, where $\mathcal{V}_{\mathcal{T}}^{\circ}$ (resp., $\mathcal{V}_{\mathcal{T}}^{\partial}$) denotes the collection of interior (resp., boundary) mesh vertices. The standard hat (Courant) basis functions are denoted as $\{\rho_{\mathbf{a}}\}_{\mathbf{a} \in \mathcal{V}_{\mathcal{T}}}$ and satisfy the partition-of-unity property $\sum_{\mathbf{a} \in \mathcal{V}_{\mathcal{T}}} \rho_{\mathbf{a}} = 1$ over Ω . We set

$$k_{\mathbf{a}\mathbf{b}} := \int_{\Omega} \nabla \rho_{\mathbf{a}} \cdot \nabla \rho_{\mathbf{b}} dx \quad \forall \mathbf{a}, \mathbf{b} \in \mathcal{V}_{\mathcal{T}}, \quad (3.1)$$

and observe that $k_{\mathbf{a}\mathbf{b}} = k_{\mathbf{b}\mathbf{a}}$ as well as $\sum_{\mathbf{a} \in \mathcal{V}_{\mathcal{T}}} k_{\mathbf{a}\mathbf{b}} = \sum_{\mathbf{b} \in \mathcal{V}_{\mathcal{T}}} k_{\mathbf{a}\mathbf{b}} = 0$ owing to the partition-of-unity property. In what follows, we assume that the triangulation \mathcal{T} is weakly acute [11, 16, 25] so that

$$k_{\mathbf{a}\mathbf{b}} \leq 0 \quad \forall \mathbf{a}, \mathbf{b} \in \mathcal{V}_{\mathcal{T}}, \mathbf{a} \neq \mathbf{b}. \quad (3.2)$$

Recall that this condition is satisfied if and only if the sum of the two angles opposite any edge connecting a pair of mesh vertices is less than or equal to π . This is a reasonable condition in 2D.

To approximate the minimization problem (2.7), we consider the discrete minimizing set

$$W_{\mathcal{T}} := \{\Phi_{\mathcal{T}} \in H^1(\Omega; \mathbb{R}^4) \mid \Phi_{\mathcal{T}}|_T \in \mathbb{P}^1(T; \mathbb{R}^4), \forall T \in \mathcal{T}; \\ \Phi_{\mathcal{T}}(\mathbf{a}) \in \mathcal{N}, \forall \mathbf{a} \in \mathcal{V}_{\mathcal{T}}^{\circ}; \Phi_{\mathcal{T}}(\mathbf{a}) = \Psi^b(\mathbf{a}), \forall \mathbf{a} \in \mathcal{V}_{\mathcal{T}}^{\partial}\}, \quad (3.3)$$

where $\mathbb{P}^1(T; \mathbb{R}^4)$ is composed of divariate, \mathbb{R}^4 -valued, affine polynomials restricted to $T \in \mathcal{T}$. We notice that every $\Phi_{\mathcal{T}} \in W_{\mathcal{T}}$ can be expanded as follows:

$$\Phi_{\mathcal{T}} = \sum_{\mathbf{a} \in \mathcal{V}_{\mathcal{T}}} \Phi_{\mathcal{T}}(\mathbf{a}) \rho_{\mathbf{a}}. \quad (3.4)$$

An important observation is the nonconforming nature of the approximation provided by the discrete minimizing set, i.e., we have $W_{\mathcal{T}} \not\subset W$. Indeed, we have $\Phi_{\mathcal{T}}(\mathbf{x}) \in \mathcal{N}$ if $\mathbf{x} \in \mathcal{V}_{\mathcal{T}}$, but this is not guaranteed if $\mathbf{x} \in \Omega \setminus \mathcal{V}_{\mathcal{T}}$. Altogether, the discrete minimization problem reads as follows:

$$\min_{\Phi_{\mathcal{T}} \in W_{\mathcal{T}}} E(\Phi_{\mathcal{T}}), \quad (3.5)$$

with the (Dirichlet) energy functional still defined in (2.6).

3.2 Preliminary notation and results

Recalling (2.2), given any $\Psi = (\Psi_1, \Psi_2, \Psi_3, \Psi_4)^{\top} \in \mathcal{N}$, we write $\mathbf{n} := M_c^{-1}(\Psi_3, \Psi_4)^{\top}$ and $\mathbf{v} := Q_c^{-1}(\Psi_1, \Psi_2)^{\top}$, so that $\mathbf{n} \in \mathcal{S}$ and $\mathbf{v} = \mathbf{R}(\mathbf{n}) \in \mathcal{S}$ as well. Consistently with this notation, for all $\Phi_{\mathcal{T}} \in W_{\mathcal{T}}$ and all $\mathbf{a} \in \mathcal{V}_{\mathcal{T}}$, we define the two vectors $\mathbf{n}(\mathbf{a})$ and $\mathbf{v}(\mathbf{a})$, both in \mathcal{S} and such that $\mathbf{v}(\mathbf{a}) = \mathbf{R}(\mathbf{n}(\mathbf{a}))$.

Lemma 3.1 (Energy evaluation). *The following holds for all $\Phi_{\mathcal{T}} \in W_{\mathcal{T}}$:*

$$\int_{\Omega} \|\nabla \Phi_{\mathcal{T}}\|_{\mathbb{R}^{4 \times 2}}^2 dx = -\frac{1}{2} \sum_{\mathbf{a}, \mathbf{b} \in \mathcal{V}_{\mathcal{T}}} k_{ab} \left\{ Q_c^2 \|\mathbf{v}(\mathbf{a}) - \mathbf{v}(\mathbf{b})\|_{\mathbb{R}^2}^2 + M_c^2 \|\mathbf{n}(\mathbf{a}) - \mathbf{n}(\mathbf{b})\|_{\mathbb{R}^2}^2 \right\}. \quad (3.6)$$

Proof. Using the expansion (3.4), the definition (3.1) of k_{ab} and the properties $\sum_{\mathbf{a} \in \mathcal{V}_{\mathcal{T}}} k_{ab} = \sum_{\mathbf{b} \in \mathcal{V}_{\mathcal{T}}} k_{ab} = 0$, we infer that

$$\begin{aligned} \int_{\Omega} \|\nabla \Phi_{\mathcal{T}}\|_{\mathbb{R}^{4 \times 2}}^2 dx &= \sum_{\mathbf{a}, \mathbf{b} \in \mathcal{V}_{\mathcal{T}}} k_{ab} \Phi_{\mathcal{T}}(\mathbf{a}) \cdot \Phi_{\mathcal{T}}(\mathbf{b}) \\ &= \frac{1}{2} \sum_{\mathbf{a}, \mathbf{b} \in \mathcal{V}_{\mathcal{T}}} k_{ab} \Phi_{\mathcal{T}}(\mathbf{a}) \cdot (\Phi_{\mathcal{T}}(\mathbf{b}) - \Phi_{\mathcal{T}}(\mathbf{a})) + \frac{1}{2} \sum_{\mathbf{a}, \mathbf{b} \in \mathcal{V}_{\mathcal{T}}} k_{ab} \Phi_{\mathcal{T}}(\mathbf{b}) \cdot (\Phi_{\mathcal{T}}(\mathbf{a}) - \Phi_{\mathcal{T}}(\mathbf{b})) \\ &= -\frac{1}{2} \sum_{\mathbf{a}, \mathbf{b} \in \mathcal{V}_{\mathcal{T}}} k_{ab} \|\Phi_{\mathcal{T}}(\mathbf{a}) - \Phi_{\mathcal{T}}(\mathbf{b})\|_{\mathbb{R}^4}^2, \end{aligned}$$

and the claim follows from $\|\Phi_{\mathcal{T}}(\mathbf{a}) - \Phi_{\mathcal{T}}(\mathbf{b})\|_{\mathbb{R}^4}^2 = Q_c^2 \|\mathbf{v}(\mathbf{a}) - \mathbf{v}(\mathbf{b})\|_{\mathbb{R}^2}^2 + M_c^2 \|\mathbf{n}(\mathbf{a}) - \mathbf{n}(\mathbf{b})\|_{\mathbb{R}^2}^2$. \square

Our second preliminary result is related to the geometry of the admissible set \mathcal{N} . We define the function $\varphi : (-1, 1) \rightarrow \mathbb{R}$ such that

$$\varphi(r) := \frac{2r}{1-r^2} \quad \forall r \in (-1, 1). \quad (3.7)$$

Lemma 3.2 (Geometry of \mathcal{N}). *Let $\mathbf{n} \in \mathcal{S}$ and let $\mathbf{t} \in T_{\mathbf{n}}\mathcal{S}$ be the unit vector obtained from \mathbf{n} by a rotation of $\frac{\pi}{2}$ in \mathbb{R}^2 . Set $\mathbf{v} := \mathbf{R}(\mathbf{n}) \in \mathcal{S}$ and let $\boldsymbol{\tau} \in T_{\mathbf{v}}\mathcal{S}$ be the unit vector obtained from \mathbf{v} by a rotation of $\frac{\pi}{2}$ in \mathbb{R}^2 . The following holds for all $r \in (-1, 1)$:*

$$(\mathbf{R} \circ P_{\mathcal{S}})(\mathbf{n} + r\mathbf{t}) = P_{\mathcal{S}}(\mathbf{v} + \varphi(r)\boldsymbol{\tau}), \quad (3.8)$$

with the function $\varphi : (-1, 1) \rightarrow \mathbb{R}$ defined in (3.7). In other words, we have

$$(Q_c P_{\mathcal{S}}(\mathbf{v} + \varphi(r)\boldsymbol{\tau}), M_c P_{\mathcal{S}}(\mathbf{n} + r\mathbf{t}))^{\top} \in \mathcal{N}. \quad (3.9)$$

Proof. We first observe that $\mathbf{n} + r\mathbf{t} \in \mathbb{R}_{\geq 1}^2$ and $\mathbf{v} + \varphi(r)\boldsymbol{\tau} \in \mathbb{R}_{\geq 1}^2$, so that both projections $P_S(\mathbf{n} + r\mathbf{t})$ and $P_S(\mathbf{v} + \varphi(r)\boldsymbol{\tau})$ are well-defined. There are many ways of verifying (3.8). We use here a representation by complex numbers. We represent \mathbf{n} as $e^{i\alpha}$ with $i^2 = -1$, $\mathbf{n} + r\mathbf{t}$ as $(1 + ir)e^{i\alpha}$, and $P_S(\mathbf{n} + r\mathbf{t})$ as $z_1 := (1 + r^2)^{-\frac{1}{2}}(1 + ir)e^{i\alpha}$. Similarly, we represent \mathbf{v} by $e^{2i\alpha}$ and $P_S(\mathbf{v} + \varphi(r)\boldsymbol{\tau})$ by $z_2 := (1 + \varphi(r)^2)^{-\frac{1}{2}}(1 + i\varphi(r))e^{2i\alpha}$. Since $|z_1| = |z_2| = 1$, the identity (3.8) amounts to $z_1^2 = z_2$. We infer that

$$\begin{aligned} z_1^2 = z_2 &\iff \frac{(1 + ir)^2}{1 + r^2} = \frac{1 + i\varphi(r)}{\sqrt{1 + \varphi(r)^2}} \\ &\iff \frac{1 - r^2}{1 + r^2} = \frac{1}{\sqrt{1 + \varphi(r)^2}} \wedge \frac{2r}{1 + r^2} = \frac{\varphi(r)}{\sqrt{1 + \varphi(r)^2}} \\ &\iff \varphi(r) := \frac{2r}{1 - r^2}. \end{aligned}$$

This completes the proof. \square

3.3 Discrete energy-decreasing algorithm

Given an initial guess $\Psi_{\mathcal{T}}^0 \in W_{\mathcal{T}}$, our goal is to generate a sequence $(\Psi_{\mathcal{T}}^j)_{j=1}^{\infty}$ in $W_{\mathcal{T}}$ that is energy-decreasing, i.e.,

$$E(\Psi_{\mathcal{T}}^{j+1}) \leq E(\Psi_{\mathcal{T}}^j). \quad (3.10)$$

At iteration $j \geq 0$, given $\Psi_{\mathcal{T}}^j \in W_{\mathcal{T}}$, we write $\Psi_{\mathcal{T}}^j(\mathbf{a}) = (Q_c \mathbf{v}^j(\mathbf{a}), M_c \mathbf{n}^j(\mathbf{a}))^T \in \mathcal{N}$ with $\mathbf{v}^j(\mathbf{a}) = \mathbf{R}(\mathbf{n}^j(\mathbf{a}))$, for all $\mathbf{a} \in \mathcal{V}_{\mathcal{T}}$, and we let $\mathbf{t}^j(\mathbf{a})$ (resp., $\boldsymbol{\tau}^j(\mathbf{a})$) be the unit vector obtained from $\mathbf{n}^j(\mathbf{a})$ (resp., $\mathbf{v}^j(\mathbf{a})$) by a rotation of $\frac{\pi}{2}$ in \mathbb{R}^2 . Set $M_{\mathcal{T}} := \mathbb{R}^{\#\mathcal{V}_{\mathcal{T}}}$ where $\#\mathcal{V}_{\mathcal{T}}$ denotes the cardinality of the set $\mathcal{V}_{\mathcal{T}}$. We define the closed convex subset

$$K_{\mathcal{T}} := \{r_{\mathcal{T}} := (r_{\mathbf{a}})_{\mathbf{a} \in \mathcal{V}_{\mathcal{T}}} \in M_{\mathcal{T}} \mid r_{\mathbf{a}} \in [-\gamma, \gamma] \forall \mathbf{a} \in \mathcal{V}_{\mathcal{T}}^{\circ}; r_{\mathbf{a}} = 0 \forall \mathbf{a} \in \mathcal{V}_{\mathcal{T}}^{\partial}\}, \quad (3.11)$$

where $\gamma \in (0, 1)$ is a user-defined parameter. Then, we define the (nonconvex) functional $F^j : K_{\mathcal{T}} \rightarrow \mathbb{R}$ such that, for all $r_{\mathcal{T}} := (r_{\mathbf{a}})_{\mathbf{a} \in \mathcal{V}_{\mathcal{T}}}$,

$$\begin{aligned} F^j(r_{\mathcal{T}}) &:= -\frac{1}{2} \sum_{\mathbf{a}, \mathbf{b} \in \mathcal{V}_{\mathcal{T}}} k_{\mathbf{ab}} \left\{ Q_c^2 \|(v^j(\mathbf{a}) + \varphi(r_{\mathbf{a}})\boldsymbol{\tau}^j(\mathbf{a})) - (v^j(\mathbf{b}) + \varphi(r_{\mathbf{b}})\boldsymbol{\tau}^j(\mathbf{b}))\|_{\mathbb{R}^2}^2 \right. \\ &\quad \left. + M_c^2 \|(n^j(\mathbf{a}) + r_{\mathbf{a}}\mathbf{t}^j(\mathbf{a})) - (n^j(\mathbf{b}) + r_{\mathbf{b}}\mathbf{t}^j(\mathbf{b}))\|_{\mathbb{R}^2}^2 \right\}. \end{aligned} \quad (3.12)$$

This functional is well-defined since $\gamma \in (0, 1)$. The algorithm proceeds in two steps:

1. We solve the minimization problem

$$r_{\mathcal{T}}^* := (r_{\mathbf{a}}^*)_{\mathbf{a} \in \mathcal{V}_{\mathcal{T}}} \in \arg \min_{r_{\mathcal{T}} \in K_{\mathcal{T}}} F^j(r_{\mathcal{T}}). \quad (3.13)$$

We refer the reader to Section 4 for algorithmic aspects of solving this problem.

2. We set, for all $\mathbf{a} \in \mathcal{V}_{\mathcal{T}}$,

$$\mathbf{n}^{j+1}(\mathbf{a}) := P_S(\mathbf{n}^j(\mathbf{a}) + r_{\mathbf{a}}^*\mathbf{t}^j(\mathbf{a})), \quad \Psi_{\mathcal{T}}^{j+1}(\mathbf{a}) := (Q_c \mathbf{R}(\mathbf{n}^{j+1}(\mathbf{a})), M_c \mathbf{n}^{j+1}(\mathbf{a}))^T. \quad (3.14)$$

(Observe that $\mathbf{n}^j(\mathbf{a}) + r_{\mathbf{a}}^*\mathbf{t}^j(\mathbf{a}) \in \mathbb{R}_{\geq 1}^2$.) By construction, $\Psi_{\mathcal{T}}^{j+1}(\mathbf{a}) \in \mathcal{N}$ for all $\mathbf{a} \in \mathcal{V}_{\mathcal{T}}$. Moreover, since $r_{\mathbf{a}}^* = 0$ for all $\mathbf{a} \in \mathcal{V}_{\mathcal{T}}^{\partial}$, we infer that $\mathbf{n}^{j+1}(\mathbf{a}) = \mathbf{n}^j(\mathbf{a})$, so that $\Psi_{\mathcal{T}}^{j+1}(\mathbf{a}) = \Psi_{\mathcal{T}}^j(\mathbf{a}) = \Psi^b(\mathbf{a})$ for all $\mathbf{a} \in \mathcal{V}_{\mathcal{T}}^{\partial}$. In conclusion, we have $\Psi_{\mathcal{T}}^{j+1} := \sum_{\mathbf{a} \in \mathcal{V}_{\mathcal{T}}} \Psi_{\mathcal{T}}^{j+1}(\mathbf{a}) \rho_{\mathbf{a}} \in W_{\mathcal{T}}$ as claimed.

Theorem 3.3 (Energy decay). *Assume that the triangulation is strictly acute so that (3.2) holds true. Then the sequence $(\Psi_{\mathcal{T}}^j)_{j=1}^{\infty}$ satisfies (3.10).*

Proof. Owing to Lemma 3.2, we infer that

$$\mathbf{v}^{j+1}(\mathbf{a}) := \mathbf{R}(\mathbf{n}^{j+1}(\mathbf{a})) = (\mathbf{R} \circ P_S)(\mathbf{n}^j(\mathbf{a}) + r_a^* \mathbf{t}^j(\mathbf{a})) = P_S(\mathbf{v}^j(\mathbf{a}) + \varphi(r_a^*) \boldsymbol{\tau}^j(\mathbf{a})).$$

Invoking Lemma 3.1 gives

$$\begin{aligned} & \int_{\Omega} \|\nabla \Psi_{\mathcal{T}}^{j+1}\|_{\mathbb{R}^{4 \times 2}}^2 \, dx \\ &= -\frac{1}{2} \sum_{\mathbf{a}, \mathbf{b} \in \mathcal{V}_{\mathcal{T}}} k_{ab} \left\{ Q_c^2 \|\mathbf{v}^{j+1}(\mathbf{a}) - \mathbf{v}^{j+1}(\mathbf{b})\|_{\mathbb{R}^2}^2 + M_c^2 \|\mathbf{n}^{j+1}(\mathbf{a}) - \mathbf{n}^{j+1}(\mathbf{b})\|_{\mathbb{R}^2}^2 \right\} \\ &= -\frac{1}{2} \sum_{\mathbf{a}, \mathbf{b} \in \mathcal{V}_{\mathcal{T}}} k_{ab} \left\{ Q_c^2 \|P_S(\mathbf{v}^j(\mathbf{a}) + \varphi(r_a^*) \boldsymbol{\tau}^j(\mathbf{a})) - P_S(\mathbf{v}^j(\mathbf{b}) + \varphi(r_b^*) \boldsymbol{\tau}^j(\mathbf{b}))\|_{\mathbb{R}^2}^2 \right. \\ &\quad \left. + M_c^2 \|P_S(\mathbf{n}^j(\mathbf{a}) + r_a^* \mathbf{t}^j(\mathbf{a})) - P_S(\mathbf{n}^j(\mathbf{b}) + r_b^* \mathbf{t}^j(\mathbf{b}))\|_{\mathbb{R}^2}^2 \right\}. \end{aligned}$$

Invoking Lemma 2.3 and crucially that $k_{ab} \leq 0$ (see (3.2)), we infer that

$$\begin{aligned} & \int_{\Omega} \|\nabla \Psi_{\mathcal{T}}^{j+1}\|_{\mathbb{R}^{4 \times 2}}^2 \, dx \\ & \leq -\frac{1}{2} \sum_{\mathbf{a}, \mathbf{b} \in \mathcal{V}_{\mathcal{T}}} k_{ab} \left\{ Q_c^2 \|(\mathbf{v}^j(\mathbf{a}) + \varphi(r_a^*) \boldsymbol{\tau}^j(\mathbf{a})) - (\mathbf{v}^j(\mathbf{b}) + \varphi(r_b^*) \boldsymbol{\tau}^j(\mathbf{b}))\|_{\mathbb{R}^2}^2 \right. \\ &\quad \left. + M_c^2 \|(\mathbf{n}^j(\mathbf{a}) + r_a^* \mathbf{t}^j(\mathbf{a})) - (\mathbf{n}^j(\mathbf{b}) + r_b^* \mathbf{t}^j(\mathbf{b}))\|_{\mathbb{R}^2}^2 \right\} \end{aligned}$$

Recalling (3.12), this proves that

$$\int_{\Omega} \|\nabla \Psi_{\mathcal{T}}^{j+1}\|_{\mathbb{R}^{4 \times 2}}^2 \, dx \leq F^j(r_{\mathcal{T}}^*).$$

Observing that $\int_{\Omega} \|\nabla \Psi_{\mathcal{T}}^j\|_{\mathbb{R}^{4 \times 2}}^2 \, dx = F^j(0)$, we conclude that

$$\int_{\Omega} \|\nabla \Psi_{\mathcal{T}}^{j+1}\|_{\mathbb{R}^{4 \times 2}}^2 \, dx \leq F^j(r_{\mathcal{T}}^*) \leq F^j(0) = \int_{\Omega} \|\nabla \Psi_{\mathcal{T}}^j\|_{\mathbb{R}^{4 \times 2}}^2 \, dx.$$

This proves the claim. \square

4 Algorithmic aspects

In this section, we provide some details on the computational algorithm for solving the minimization problem (3.13), followed by an overall description of the energy-decreasing iterative procedure.

4.1 Decomposition-coordination principle using augmented Lagrangian

To tackle the minimization problem (3.13), we employ a decomposition-coordination strategy based on an augmented Lagrangian framework. The idea is to introduce the auxiliary variable $p_a = \varphi(r_a)$ for all $\mathbf{a} \in \mathcal{V}_{\mathcal{T}}$, which we rewrite in more compact form as $p_{\mathcal{T}} = \varphi(r_{\mathcal{T}}) \in M_{\mathcal{T}}$. The idea is then to consider a minimization problem in the two variables $r_{\mathcal{T}} := (r_a)_{\mathbf{a} \in \mathcal{V}_{\mathcal{T}}} \in K_{\mathcal{T}}$ and $p_{\mathcal{T}} := (p_a)_{\mathbf{a} \in \mathcal{V}_{\mathcal{T}}} \in M_{\mathcal{T}}$ (decomposition step), and to enforce that $p_{\mathcal{T}} = \varphi(r_{\mathcal{T}})$ by means of a Lagrange multiplier $\lambda_{\mathcal{T}} = (\lambda_a)_{\mathbf{a} \in \mathcal{V}_{\mathcal{T}}} \in M_{\mathcal{T}}$ and an augmented Lagrangian (coordination step).

In the first step, recalling the cost functional F^j in (3.12), we set

$$F_1^j(r_{\mathcal{T}}) := -\frac{1}{2} \sum_{\mathbf{a}, \mathbf{b} \in \mathcal{V}_{\mathcal{T}}} k_{ab} M_c^2 \|(\mathbf{n}^j(\mathbf{a}) + r_a \mathbf{t}^j(\mathbf{a})) - (\mathbf{n}^j(\mathbf{b}) + r_b \mathbf{t}^j(\mathbf{b}))\|_{\mathbb{R}^2}^2, \quad (4.1a)$$

$$F_2^j(p_{\mathcal{T}}) := -\frac{1}{2} \sum_{\mathbf{a}, \mathbf{b} \in \mathcal{V}_{\mathcal{T}}} k_{ab} Q_c^2 \|(\mathbf{v}^j(\mathbf{a}) + p_a \boldsymbol{\tau}^j(\mathbf{a})) - (\mathbf{v}^j(\mathbf{b}) + p_b \boldsymbol{\tau}^j(\mathbf{b}))\|_{\mathbb{R}^2}^2, \quad (4.1b)$$

so that $F_1^j(r_{\mathcal{T}}) + F_2^j(p_{\mathcal{T}}) = F^j(r_{\mathcal{T}})$ whenever $p_{\mathcal{T}} = \varphi(r_{\mathcal{T}})$. For later use, we record the expressions for the gradients of the above two functionals: For all $\mathbf{a} \in \mathcal{V}_{\mathcal{T}}$,

$$\nabla_{r_{\mathbf{a}}} F_1^j(\tilde{r}_{\mathcal{T}}) = -2 \sum_{\mathbf{b} \in \mathcal{V}_{\mathcal{T}}} k_{ab} M_c^2 (\tilde{r}_{\mathbf{a}} - \tilde{r}_{\mathbf{b}} \mathbf{t}^j(\mathbf{a}) \cdot \mathbf{t}^j(\mathbf{b}) - \mathbf{t}^j(\mathbf{a}) \cdot \mathbf{n}^j(\mathbf{b})), \quad (4.2a)$$

$$\nabla_{p_{\mathbf{a}}} F_2^j(\tilde{p}_{\mathcal{T}}) = -2 \sum_{\mathbf{b} \in \mathcal{V}_{\mathcal{T}}} k_{ab} Q_c^2 (\tilde{p}_{\mathbf{a}} - \tilde{p}_{\mathbf{b}} \boldsymbol{\tau}^j(\mathbf{a}) \cdot \boldsymbol{\tau}^j(\mathbf{b}) - \boldsymbol{\tau}^j(\mathbf{a}) \cdot \boldsymbol{\nu}^j(\mathbf{b})). \quad (4.2b)$$

Then the decomposed version of the minimization problem (3.13) reads as

$$\min_{\substack{(r_{\mathcal{T}}, p_{\mathcal{T}}) \in K_{\mathcal{T}} \times M_{\mathcal{T}} \\ p_{\mathcal{T}} = \varphi(r_{\mathcal{T}})}} \left\{ F_1^j(r_{\mathcal{T}}) + F_2^j(p_{\mathcal{T}}) \right\}. \quad (4.3)$$

In the second step, the constraint in (4.3) is enforced using a Lagrange multiplier $\lambda_{\mathcal{T}} \in M_{\mathcal{T}}$. We define the Lagrangian on $K_{\mathcal{T}} \times M_{\mathcal{T}} \times M_{\mathcal{T}}$ such that

$$L^j(r_{\mathcal{T}}, p_{\mathcal{T}}, \lambda_{\mathcal{T}}) = F_1^j(r_{\mathcal{T}}) + F_2^j(p_{\mathcal{T}}) + \lambda_{\mathcal{T}}^T D(p_{\mathcal{T}} - \varphi(r_{\mathcal{T}})). \quad (4.4)$$

Here, D is a diagonal matrix with entries $(d_{\mathbf{a}})_{\mathbf{a} \in \mathcal{V}_{\mathcal{T}}}$ that is expected to scale as the entries k_{ab} of the stiffness matrix so as to balance dimensionally all the terms on the above right-hand side. In the present two-dimensional setting, a reasonable choice is $d_{\mathbf{a}} := h^{d-2} = 1$ for all $\mathbf{a} \in \mathcal{V}_{\mathcal{T}}$, where h denotes the mesh size (the largest element diameter in \mathcal{T}). We work with an augmented Lagrangian formulation. Given the augmentation parameter $\zeta > 0$, we set

$$L_{\zeta}^j(r_{\mathcal{T}}, p_{\mathcal{T}}, \lambda_{\mathcal{T}}) = F_1^j(r_{\mathcal{T}}) + F_2^j(p_{\mathcal{T}}) + \lambda_{\mathcal{T}}^T D(p_{\mathcal{T}} - \varphi(r_{\mathcal{T}})) + \frac{\zeta}{2} (p_{\mathcal{T}} - \varphi(r_{\mathcal{T}}))^T D(p_{\mathcal{T}} - \varphi(r_{\mathcal{T}})). \quad (4.5)$$

Set $u_{\mathcal{T}} := (r_{\mathcal{T}}, p_{\mathcal{T}}) \in K_{\mathcal{T}} \times M_{\mathcal{T}}$. A couple $(u_{\mathcal{T}}, \lambda_{\mathcal{T}})$ is a saddle-point of the augmented Lagrangian L_{ζ}^j if and only if

$$L_{\zeta}^j(u_{\mathcal{T}}, \theta_{\mathcal{T}}) \leq L_{\zeta}^j(u_{\mathcal{T}}, \lambda_{\mathcal{T}}) \leq L_{\zeta}^j(v_{\mathcal{T}}, \lambda_{\mathcal{T}}) \quad \forall \theta_{\mathcal{T}} \in M_{\mathcal{T}}, \forall v_{\mathcal{T}} \in K_{\mathcal{T}} \times M_{\mathcal{T}}. \quad (4.6)$$

Our goal is now to find a saddle-point of L_{ζ}^j . We do so by using an alternating-direction Uzawa-like iterative method that we describe next.

4.2 Alternating-direction Uzawa-like iterations

We find a saddle-point of L_{ζ}^j by means of the Uzawa/Alternating Direction Method of Multipliers (ADMM) [2, 17]. The iterative method is initialized by specifying $p_{\mathcal{T}}^0 \in M_{\mathcal{T}}$ and $\lambda_{\mathcal{T}}^0 \in M_{\mathcal{T}}$ (see Remark 4.1 below). Then, at iteration $n \geq 0$, assuming $p_{\mathcal{T}}^n, \lambda_{\mathcal{T}}^n$ known from the initialization or the previous iteration, we calculate $r_{\mathcal{T}}^{n+1} \in K_{\mathcal{T}}$, then $p_{\mathcal{T}}^{n+1} \in M_{\mathcal{T}}$ and finally $\lambda_{\mathcal{T}}^{n+1} \in M_{\mathcal{T}}$ in the following three steps:

$$r_{\mathcal{T}}^{n+1} \leftarrow \arg \min_{r_{\mathcal{T}} \in K_{\mathcal{T}}} L_{\zeta}^j(r_{\mathcal{T}}, p_{\mathcal{T}}^n, \lambda_{\mathcal{T}}^n), \quad (4.7a)$$

$$p_{\mathcal{T}}^{n+1} \leftarrow \arg \min_{p_{\mathcal{T}} \in M_{\mathcal{T}}} L_{\zeta}^j(r_{\mathcal{T}}^{n+1}, p_{\mathcal{T}}, \lambda_{\mathcal{T}}^n), \quad (4.7b)$$

$$\lambda_{\mathcal{T}}^{n+1} \leftarrow \lambda_{\mathcal{T}}^n + \rho \nabla_{\lambda} L_{\zeta}^j(r_{\mathcal{T}}^{n+1}, p_{\mathcal{T}}^{n+1}, \lambda_{\mathcal{T}}), \quad (4.7c)$$

where $\rho > 0$ is a user-dependent parameter.

Let us briefly describe the three steps in (4.7), starting with the second step (4.7b) which simply amounts to a linear solve: Find $p_{\mathcal{T}}^{n+1} \in M_{\mathcal{T}}$ so that

$$\nabla_{p_{\mathbf{a}}} L_{\zeta}^j(r_{\mathcal{T}}^{n+1}, p_{\mathcal{T}}^{n+1}, \lambda_{\mathcal{T}}^n) = \nabla_{p_{\mathbf{a}}} F_2^j(p_{\mathcal{T}}^{n+1}) + d_{\mathbf{a}} \lambda_{\mathcal{T}}^n + \zeta d_{\mathbf{a}} (p_{\mathbf{a}}^{n+1} - \varphi(r_{\mathbf{a}}^{n+1})) = 0, \quad \forall \mathbf{a} \in \mathcal{V}_{\mathcal{T}}, \quad (4.8)$$

where the gradient of F_2^j is given by (4.2b). The third step, (4.7c), in turn amounts to a simple componentwise update on the Lagrange multiplier by setting

$$\lambda_a^{n+1} = \lambda_a^n + \rho d_a (p_a^{n+1} - \varphi(r_a^{n+1})), \quad \forall a \in \mathcal{V}_{\mathcal{T}}. \quad (4.9)$$

Finally, the first step, (4.7a), is more intricate owing to the nonlinearity produced by the function φ . The idea to enhance computational efficiency is then to replace, only in the first step (4.7a), the nonlinear function φ by its linearization at $r_{\mathcal{T}}^n$ given by $\varphi_L^n(r_{\mathcal{T}}) := \varphi(r_{\mathcal{T}}^n) + \varphi'(r_{\mathcal{T}}^n)(r_{\mathcal{T}} - r_{\mathcal{T}}^n)$. With the same goal in mind, we also relax the constraint of seeking a minimizer in $K_{\mathcal{T}}$, and just seek a minimizer in $M_{\mathcal{T}}$ (this is possible since the linearized function φ_L is defined over the whole real line). Our numerical experiments below indicate that the obtained minimizer anyway lies in $K_{\mathcal{T}}$ (see Remark 4.2 below for further discussion). Altogether, the first step (4.7a) is replaced by

$$r_{\mathcal{T}}^{n+1} \leftarrow \arg \min_{r_{\mathcal{T}} \in M_{\mathcal{T}}} L_{L,\zeta}^{j,n}(r_{\mathcal{T}}, p_{\mathcal{T}}^n, \lambda_{\mathcal{T}}^n), \quad (4.10)$$

with the linearized augmented Lagrangian

$$L_{L,\zeta}^{j,n}(r_{\mathcal{T}}, p_{\mathcal{T}}, \lambda_{\mathcal{T}}) = F_1^j(r_{\mathcal{T}}) + F_2^j(p_{\mathcal{T}}) + \lambda_{\mathcal{T}}^T D(p_{\mathcal{T}} - \varphi_L^n(r_{\mathcal{T}})) + \frac{\zeta}{2} (p_{\mathcal{T}} - \varphi_L^n(r_{\mathcal{T}}))^T D(p_{\mathcal{T}} - \varphi_L^n(r_{\mathcal{T}})). \quad (4.11)$$

A straightforward calculation shows that (4.10) amounts to the following linear solve: Find $r_{\mathcal{T}}^{n+1} \in M_{\mathcal{T}}$ so that, for all $a \in \mathcal{V}_{\mathcal{T}}$,

$$\begin{aligned} \nabla_{r_a} L_{L,\zeta}^{j,n}(r_{\mathcal{T}}^{n+1}, p_{\mathcal{T}}^n, \lambda_{\mathcal{T}}^n) &= \nabla_{r_a} F_1^j(r_{\mathcal{T}}^{n+1}) - d_a \lambda_a^n \varphi'(r_a^n) \\ &\quad - \zeta d_a (p_a^n - \varphi(r_a^n) - \varphi'(r_a^n)(r_a^{n+1} - r_a^n)) \varphi'(r_a^n) = 0, \end{aligned} \quad (4.12)$$

where the gradient of F_1^j is given by (4.2a). The linearization in (4.10) is consistent since $L_{L,\zeta}^{j,n} \rightarrow L_{L,\zeta}^j$ in the limit $n \rightarrow \infty$. We emphasize that the nonlinear function φ is still used in (4.7b) and in (4.7c). In particular, if the Uzawa-like iteration converges, (4.9) guarantees that $p_a^{n+1} = \varphi(r_a^{n+1})$, which is the critical condition required to ensure an energy decrease. We notice in passing that one consequence of the above linearization is the need to provide a value for the initial primal variable, $r_{\mathcal{T}}^0$.

Remark 4.1 (Initialization). We initialize the Uzawa/ADMM iterations in a nested fashion by exploiting the outer energy-decreasing loop (index j). At iteration j , we set $r_{\mathcal{T}}^0 := r_{\mathcal{T}}^{j-1,*}$, $p_{\mathcal{T}}^0 := p_{\mathcal{T}}^{j-1,*}$ and $\lambda_{\mathcal{T}}^0 := \lambda_{\mathcal{T}}^{j-1,*}$, where the right-hand sides are the values obtained at convergence of the Uzawa/ADMM algorithm at the previous iteration ($j-1$). For $j=0$, we simply set $r_{\mathcal{T}}^0 := 0$, $p_{\mathcal{T}}^0 := 0$ and $\lambda_{\mathcal{T}}^0 := 0$.

Remark 4.2 (Domain of $r_{\mathcal{T}}$). The above alternating-direction Uzawa-like iteration does not guarantee that the discrete variable $r_{\mathcal{T}}$ lies within the admissible interval $(-1, 1)$. It turns out to be the case in all our numerical experiments. We notice that the variable $r_{\mathcal{T}}$ is related to the step-size in the energy-decreasing algorithm, so that it is expected to tend to zero if convergence does indeed occur. Therefore, possible difficulties with the domain of $r_{\mathcal{T}}$ are to be expected, if any, at the first iterations. It is possible to add an energy barrier to the Lagrangian so as to prevent $r_{\mathcal{T}}$ from stepping out of its admissible domain. One possibility is to consider the Lagrangian (we omit the augmentation term for brevity)

$$L^j(r_{\mathcal{T}}, p_{\mathcal{T}}, \lambda_{\mathcal{T}}) = F_1^j(r_{\mathcal{T}}) + F_2^j(p_{\mathcal{T}}) + \lambda_{\mathcal{T}}^T D(p_{\mathcal{T}} - \varphi(r_{\mathcal{T}})) + \sum_{a \in \mathcal{V}_{\mathcal{T}}} s_a \log |1 - r_a^2|,$$

where $(s_a)_{a \in \mathcal{V}_{\mathcal{T}}}$ is a collection of user-dependent weights. As the introduction of the energy barrier in the Lagrangian makes the first step, (4.7a), of the Uzawa-like algorithm nonlinear, the linearization of the coupling function φ is no longer relevant. The nonlinear minimization problem to evaluate $r_{\mathcal{T}}^{n+1}$ can be implemented using a gradient-descent iterative scheme combined, e.g., with Armijo's rule for line-search at each step. Details are omitted for brevity as this algorithm is classical.

4.3 Overall computational algorithm

The pseudocode in Algorithm 1 describes the computational workflow. The method employs a nested iterative structure, where the outer loop (index j) performs energy-descent updates, whereas the inner loop (index n) solves the associated constrained minimization problem using the alternating-direction Uzawa-like iteration described in the previous section. The stopping criterion for the outer energy-decreasing loop is

$$-\varepsilon_0 \varepsilon_{\text{outer}} \leq E(\Psi_{\mathcal{T}}^j) - E(\Psi_{\mathcal{T}}^{j+1}) \leq \varepsilon_{\text{outer}} \quad (4.13)$$

with tolerance $\varepsilon_{\text{outer}} := 10^{-6}$. We allow for a slightly negative lower bound in (4.13) with $\varepsilon_0 := 10^{-3}$ in order to avoid pursuing further iterations when the energy essentially stagnates. The stopping criterion for the inner Uzawa/ADMM loop is based on the satisfaction of the coupling condition $p_{\mathcal{T}} = \varphi(r_{\mathcal{T}})$ and reads as follows:

$$\left(\frac{1}{\#\mathcal{V}_{\mathcal{T}}} \sum_{\mathbf{a} \in \mathcal{V}_{\mathcal{T}}} |\varphi(r_{\mathbf{a}}^{n+1}) - p_{\mathbf{a}}^{n+1}|^2 \right)^{\frac{1}{2}} \leq \varepsilon_{\text{pri}}. \quad (4.14)$$

The tolerance ε_{pri} can vary across the numerical experiments and is specified in Section 5. All the linear systems arising in the Uzawa/ADMM loop are solved by a direct method using QR decomposition.

Algorithm 1: Energy-descent with embedded Uzawa-like algorithm

Input: Initial approximation $\Psi_{\mathcal{T}}^0 \in W_{\mathcal{T}}$ on triangulation \mathcal{T}

- 1 **for** $j = 0, 1, 2, \dots$ **do**
- 2 **Step 1:** Given $\Psi_{\mathcal{T}}^j \in W_{\mathcal{T}}$, solve (3.13) for $r_{\mathcal{T}}^* \in K_{\mathcal{T}}$ using Uzawa/ADMM;
- 3 **Initialize Uzawa variables:** $r_{\mathcal{T}}^0 := r_{\mathcal{T}}^{j-1}$, $p_{\mathcal{T}}^0 := p_{\mathcal{T}}^{j-1}$, and $\lambda_{\mathcal{T}}^0 := \lambda_{\mathcal{T}}^{j-1}$ if $j \geq 1$ or $r_{\mathcal{T}}^0 := 0$, $p_{\mathcal{T}}^0 := 0$, $\lambda_{\mathcal{T}}^0 := 0$ otherwise ;
- 4 **for** $n = 0, 1, \dots$ **do**
- 5 Step 1.1 (Primal Variable Update). Compute $r_{\mathcal{T}}^{n+1}$ from (4.10);
- 6 Step 1.2 (Auxiliary Variable Update). Compute $p_{\mathcal{T}}^{n+1}$ from (4.8);
- 7 Step 1.3 (Lagrange multiplier Update). Compute $\lambda_{\mathcal{T}}^{n+1}$ from (4.9);
- 8 **if** (4.14) *holds* **then**
- 9 **break** ; // Terminate Uzawa/ADMM iterations
- 10 **Step 2:** For all $\mathbf{a} \in \mathcal{V}_{\mathcal{T}}$, compute $\Psi_{\mathcal{T}}^{j+1}(\mathbf{a})$ as in (3.14).
- 11 **if** (4.13) *holds* **then**
- 12 **break** ; // Terminate outer iterations

Output: Discrete approximation $\Psi_{\mathcal{T}}^{j+1}$ and discrete energy $E(\Psi_{\mathcal{T}}^{j+1})$

5 Numerical results

This section presents computational experiments on two test cases with known analytical solution. The goal is to illustrate the performances of the present methodology in terms of efficiency and accuracy. In all cases, we consider the square domain $\Omega := (0, 1)^2$ and discretize it using four successively refined, unstructured triangulations of size $h \in \{0.1270, 0.0635, 0.0318, 0.0159\}$ (the diameter of the largest triangle in each triangulation). These triangulations are, respectively, called \mathcal{T}_1 , \mathcal{T}_2 , \mathcal{T}_3 , and \mathcal{T}_4 . These triangulations are all weakly acute so that (3.2) always holds true. The finest triangulation, \mathcal{T}_4 , is only considered for the second test case which is more challenging.

The ferromagnetic parameters are set to $Q_c := \left(c/4 + \chi\right)^{\frac{1}{3}} + \left(c/4 - \chi\right)^{\frac{1}{3}}$, $\chi := (c^2/16 - (1 + c^2/2)^3/27)^{\frac{1}{2}}$, and $M_c := (1 + cQ_c)^{\frac{1}{2}}$ (see [14]) with $c := 0.005$, giving $Q_c \approx 1.0013$ and $M_c \approx 1.0025$. To define the analytical solution, we consider the map $\Phi : \mathbb{R}^2 \times \mathbb{R}^2 \rightarrow \mathbb{R}^4$ such that $\Phi(\mathbf{X}; \mathbf{x}) = \mathcal{G}(\bar{\mathbf{n}}(\mathbf{X}; \mathbf{x}))$

with $\tilde{\mathbf{n}}(X; \mathbf{x}) := -\frac{(\mathbf{x}-X)^\perp}{\|\mathbf{x}-X\|_{\mathbb{R}^2}}$ for all $\mathbf{x} \neq X$. Choosing $\mathbf{x}_0 \notin \Omega$ leads to the (smooth) analytical solution $\Psi_{\mathbf{x}_0}(\mathbf{x}) := \Phi(\mathbf{x}_0, \mathbf{x})$ for all $\mathbf{x} \in \Omega$. In our numerical experiments, the analytical solution is only used to define the boundary datum Ψ^b (and to compute the errors). We denote by $\Psi_{\mathcal{T}_i}^{\text{cv}}$ the converged solution on the mesh $\mathcal{T}_i, i \in \{1, 2, 3, 4\}$.

5.1 Example 1

We define the boundary datum Ψ^b using $\mathbf{x}_0 = (2, 0.2)^\top$. Figure 1 displays the two components \mathbf{Q} and \mathbf{M} of the exact solution $\Psi_{\mathbf{x}_0}$. For reference, we have $E(\Psi_{\mathbf{x}_0}) \approx 1.15113$.

To initialize the energy-decreasing iterations, we set $\Psi^0(\mathbf{x}) := \Phi(Y(\mathbf{x}); \mathbf{x})$ for all $\mathbf{x} \in \Omega$, with $Y(\mathbf{x}) = (1 - \delta(\mathbf{x}))\mathbf{x}_0 + \delta(\mathbf{x})\mathbf{x}_1$ for $\mathbf{x}_1 \notin \Omega$ and $\delta(\mathbf{x}) := \rho_\Omega^{-1} \text{dist}(\mathbf{x}, \partial\Omega)$ where $\rho_\Omega := \max_{\mathbf{x} \in \Omega} \text{dist}(\mathbf{x}, \partial\Omega)$. Notice that $Y(\mathbf{x}) = \mathbf{x}_0$ for all $\mathbf{x} \in \partial\Omega$ so that $\Psi^0|_{\partial\Omega} = \Psi^b$. We set $\mathbf{x}_1 = (1.5, 1.5)^\top$.

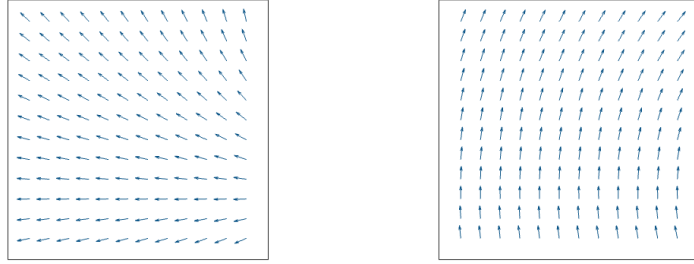


Figure 1: Nematic profile \mathbf{Q} (left) and magnetic profile \mathbf{M} (right) for the exact solution $\Psi_{\mathbf{x}_0}$ with $\mathbf{x}_0 = (2, 0.2)^\top$; the domain is $\Omega := (0, 1)^2$.

	$\mathcal{T}_1 (\times 10^{-3})$			$\mathcal{T}_2 (\times 10^{-3})$			$\mathcal{T}_3 (\times 10^{-4})$		
$\zeta \setminus \rho$	1	0.5	0.25	1	0.5	0.25	1	0.5	0.25
	$\varepsilon_{\text{pri}} = 10^{-6}$								
1	9.44	2.74	1.01	0.47	0.33	0.20	0.41	0.37	0.31
4	0.47	0.40	0.38	0.10	0.10	0.09	0.64	0.60	0.25
16	0.37	0.37	0.37	0.09	0.09	0.09	0.93	0.24	0.24
	$\varepsilon_{\text{pri}} = 10^{-7}$								
1	9.44	2.74	1.02	0.47	0.32	0.20	0.30	0.30	0.30
4	0.47	0.40	0.38	0.10	0.10	0.09	0.30	0.27	0.26
16	0.37	0.37	0.37	0.10	0.09	0.09	0.57	0.28	0.29
	$\varepsilon_{\text{pri}} = 10^{-8}$								
1	9.44	2.74	1.02	0.47	0.32	0.20	0.30	0.30	0.29
4	0.47	0.40	0.38	0.10	0.10	0.09	0.24	0.24	0.24
16	0.37	0.37	0.37	0.09	0.09	0.09	0.26	0.28	0.24

Table 1: Final energy error $\Delta E_i := E(\Psi_{\mathcal{T}_i}^{\text{cv}}) - E(\Psi_{\mathbf{x}_0})$ on the first three triangulations, $i \in \{1, 2, 3\}$, and for various choices of the Uzawa/ADMM parameters: $\zeta \in \{1, 4, 16\}$, $\rho \in \{1, 0.5, 0.25\}$, $\varepsilon_{\text{pri}} \in \{10^{-6}, 10^{-7}, 10^{-8}\}$.

We first study how the three parameters driving the Uzawa/ADMM iterations, namely the augmentation parameter ζ , the update parameter ρ , and the Uzawa/ADMM tolerance ε_{pri} , influence the convergence behavior and the accuracy of the overall algorithm. Table 1 reports the errors in the predicted energy value at convergence of the overall algorithm, $\Delta E_i := E(\Psi_{\mathcal{T}_i}^{\text{cv}}) - E(\Psi_{\mathbf{x}_0})$. Our numerical experiments indicate that ΔE_i always takes positive values. This is not guaranteed a priori as the discrete minimizing set is not a subset of the exact one. To drive the Uzawa/ADMM iterations, we consider the values $\zeta \in \{1, 4, 16\}$, $\rho \in \{1, 0.5, 0.25\}$, $\varepsilon_{\text{pri}} \in \{10^{-6}, 10^{-7}, 10^{-8}\}$, and the first three triangulations $\mathcal{T}_1, \mathcal{T}_2$, and

\mathcal{T}_3 . The following comments can be made from the results reported in Table 1. Comparing the three meshes, the final energy error ΔE_i is reduced as the mesh is refined, confirming that discretization errors are under control. Focusing now on the Uzawa/ADMM tolerance, we observe that, on the finest mesh, \mathcal{T}_3 , the final energy error ΔE_3 takes close values for the two tighter tolerances, $\varepsilon_{\text{pri}} \in \{10^{-7}, 10^{-8}\}$, whereas it is larger when $\varepsilon_{\text{pri}} = 10^{-6}$. This suggests to choose $\varepsilon_{\text{pri}} \leq 10^{-7}$ when using \mathcal{T}_3 . Instead, on \mathcal{T}_1 and \mathcal{T}_2 , the final energy error ΔE_i , $i \in \{1, 2\}$, is the same for the three considered values of ε_{pri} , suggesting to choose $\varepsilon_{\text{pri}} \leq 10^{-6}$ for the two coarser meshes. Finally, when reaching low values for the final energy error, the choice of the parameters ζ and ρ is not that significant as far as accuracy is concerned. Instead, when the error is larger, as on \mathcal{T}_1 , larger values for ζ are to be preferred to achieve tighter errors.

	\mathcal{T}_1			\mathcal{T}_2			\mathcal{T}_3		
$\zeta \setminus \rho$	1	0.5	0.25	1	0.5	0.25	1	0.5	0.25
	$\varepsilon_{\text{pri}} = 10^{-6}$								
1	3(1)	6(2)	3(1)	4	8	5(1)	13	8	9
4	4(1)	4	2	7	5	5	47(1)	0	61(10)
16	6	3	3	60(9)	43(10)	30(8)	347(27)	397(42)	230(33)
	$\varepsilon_{\text{pri}} = 10^{-7}$								
1	2	2	2	2	4	2	8	4	3
4	2	4	2	2	2	2	12	8	7
16	2	2	2	6	6	5	39	64(7)	29(2)
	$\varepsilon_{\text{pri}} = 10^{-8}$								
1	3	3	2	2	3	2	2	2	2
4	3	2	3	2	3	2	4	4	3
16	3	2	2	3	2	2	12	6	8

Table 2: Total number of outer iterations (with total number of oscillations in parentheses, only whenever nonzero) on the three triangulations and for various choices of the Uzawa/ADMM parameters: $\zeta \in \{1, 4, 16\}$, $\rho \in \{1, 0.5, 0.25\}$, $\varepsilon_{\text{pri}} \in \{10^{-6}, 10^{-7}, 10^{-8}\}$.

Another way of looking at how an insufficient resolution in the Uzawa/ADMM iterations affects the behavior of the outer iterations is to check whether the outer loop does indeed achieve an energy decrease at each iteration j . Non-optimal choices of the parameters ζ , ρ , and ε_{pri} may induce oscillations in the energy decay, as quantified in Table 2. Some oscillations in the energy decay are observed for $\varepsilon_{\text{pri}} = 10^{-6}$ on \mathcal{T}_1 and on \mathcal{T}_2 , and for $\varepsilon_{\text{pri}} \in \{10^{-6}, 10^{-7}\}$ on \mathcal{T}_3 . These oscillations disappear when utilizing tighter tolerances. Thus, strict energy decay can be achieved by utilizing sufficiently tight tolerances in the Uzawa/ADMM iterations.

Table 3 reports the cumulative (across the whole outer iteration) number of Uzawa/ADMM iterations for the different choices of ζ , ρ , and ε_{pri} considered above and for the three triangulations. An increase in the number of Uzawa/ADMM iterations is observed (as expected) with mesh refinement and when making the tolerance ε_{pri} tighter. Another observation is that the augmentation parameter ζ has a strong influence on the iteration count: larger values (for example $\zeta = 16$) lead to (much) more iterations across all meshes. The effect of ρ is comparatively milder, though smaller values tend to slightly increase the iteration count. The lowest values of the iteration count are marked in green in Table 3 for each value of ε_{pri} and each mesh. In all cases, the lowest iteration count is observed for $(\zeta, \rho) = (1, 1)$.

Figure 2 illustrates the trade-off between accuracy and computational cost by combining the results reported in Tables 1 and 3. The tolerance is set to $\varepsilon_{\text{pri}} = 10^{-7}$ on the meshes \mathcal{T}_1 and \mathcal{T}_2 and $\varepsilon_{\text{pri}} = 10^{-8}$ on the mesh \mathcal{T}_3 . Only three simulations lead to a cumulative iteration count below 100, those on \mathcal{T}_1 with $\zeta = 1$. The corresponding energy error ΔE_1 is still fairly large, and takes smaller values by decreasing ρ . We also observe that the accuracy to cost ratio achieved on \mathcal{T}_1 using $\zeta = 4$ and on \mathcal{T}_2 using $\zeta = 1$ is about the same. Finally, as expected, the better errors are obtained at the price of a stronger computational effort, but an interesting observation is that increasing the value of ζ is not beneficial in terms of accuracy/cost trade-off, as the accuracy only slightly improves, but the cost swiftly increases for larger values of ζ .

	\mathcal{T}_1			\mathcal{T}_2			\mathcal{T}_3		
$\zeta \setminus \rho$	1	0.5	0.25	1	0.5	0.25	1	0.5	0.25
	$\varepsilon_{\text{pri}} = 10^{-6}$								
1	53	63	64	143	171	180	426	444	500
4	181	183	175	482	520	541	1541	1580	1953
16	564	510	511	1956	1962	1892	6080	6844	6630
	$\varepsilon_{\text{pri}} = 10^{-7}$								
1	67	73	68	171	190	199	518	554	573
4	200	231	213	574	594	652	1764	1875	1951
16	619	640	660	1954	2033	1964	6311	7418	6989
	$\varepsilon_{\text{pri}} = 10^{-8}$								
1	77	83	88	190	236	255	629	665	720
4	256	259	279	721	796	818	2130	2277	2354
16	841	807	827	2211	2437	2368	7557	7418	8015

Table 3: Total number of Uzawa/ADMM iterations on the three triangulations and for various choices of the Uzawa/ADMM parameters: $\zeta \in \{1, 4, 16\}$, $\rho \in \{1, 0.5, 0.25\}$, $\varepsilon_{\text{pri}} \in \{10^{-6}, 10^{-7}, 10^{-8}\}$.

Altogether, the results of Figure 2 suggest the following choices of parameters: $\zeta = 16$, $\rho = 1$, $\varepsilon_{\text{pri}} = 10^{-7}$ on \mathcal{T}_1 , $\zeta = 4$, $\rho = 1$, $\varepsilon_{\text{pri}} = 10^{-7}$ on \mathcal{T}_2 , and $\zeta = 1$, $\rho = 1$, $\varepsilon_{\text{pri}} = 10^{-8}$ on \mathcal{T}_3 .

i	$E(\Psi_{x_0})$	$E(\Psi_{x_0}^I)$	$E(\Psi_{\mathcal{T}_i}^{\text{cv}})$	ΔE_i	rate	$j \setminus i$	1	2	3
1	1.151	1.152	1.152	3.69×10^{-4}	–	0	8.872	9.32	9.52
2	1.151	1.151	1.151	9.93×10^{-5}	1.98	1	3.69×10^{-4}	9.96×10^{-5}	2.98×10^{-5}
3	1.151	1.151	1.151	2.98×10^{-5}	1.74	2	3.69×10^{-4}	9.93×10^{-5}	2.98×10^{-5}

Table 4: Left: exact energy $E(\Psi_{x_0})$, energy for the nodal interpolation of the exact solution, $E(\Psi_{x_0}^I)$, and computed energy $E(\Psi_{\mathcal{T}_i}^{\text{cv}})$ at convergence, together with the error $\Delta E_i := E(\Psi_{\mathcal{T}_i}^{\text{cv}}) - E(\Psi_{x_0})$ and convergence rates, for the three triangulations \mathcal{T}_i , $i \in \{1, 2, 3\}$. Right: Energy error $\Delta E_i^j := E(\Psi_{\mathcal{T}_i}^j) - E(\Psi_{x_0})$ for the outer iteration index $j \in \{0, 1, 2\}$ and the mesh index $i \in \{1, 2, 3\}$.

i	H^1 -seminorm	rate	L^2 -norm	rate
1	6.79×10^{-2}	–	1.51×10^{-3}	–
2	3.41×10^{-2}	0.99	6.57×10^{-4}	1.20
3	1.74×10^{-2}	0.98	4.03×10^{-4}	0.70

Table 5: Errors in energy- and L^2 -norm on $\Psi_{\mathcal{T}_i}^{\text{cv}}$ and convergence rates.

Table 4 (left) reports the exact energy $E(\Psi_{x_0})$ (computed using a sixth-order quadrature on each mesh), the energy $E(\Psi_{x_0}^I)$ for the nodal interpolation $\Psi_{x_0}^I$ of the exact solution Ψ_{x_0} , and the final discrete energy $E(\Psi_{\mathcal{T}_i}^{\text{cv}})$ computed for the above choices of the Uzawa/ADAM parameters and tolerances for each triangulation \mathcal{T}_i , $i \in \{1, 2, 3\}$. We also report the corresponding energy errors ΔE_i and convergence rates. We observe that the energy $E(\Psi_{x_0}^I)$ using nodal interpolation provides an upper bound on the exact energy, $E(\Psi_{x_0})$, in this example. However, this is not expected in general due to the nonconforming discretization of the constraint manifold \mathcal{N} . Table 4 (right) displays the energy errors $\Delta E_i^j := E(\Psi_{\mathcal{T}_i}^j) - E(\Psi_{x_0})$ as a function of the outer iteration index $j \in \{0, 1, 2\}$ and the mesh index $i \in \{1, 2, 3\}$. On the three triangulations, the outer iteration converges at $j = 2$, and the improvement in energy error as the mesh is refined is clearly visible. Table 5 presents the errors on $\Psi_{\mathcal{T}_i}^{\text{cv}}$ evaluated in the H^1 -seminorm and in the L^2 -norm, together with the corresponding convergence rates. First-order convergence is observed for both norms, which is the expected rate for the H^1 -seminorm. It is not clear that an improved rate can be achieved in the L^2 -norm as no duality argument is available.

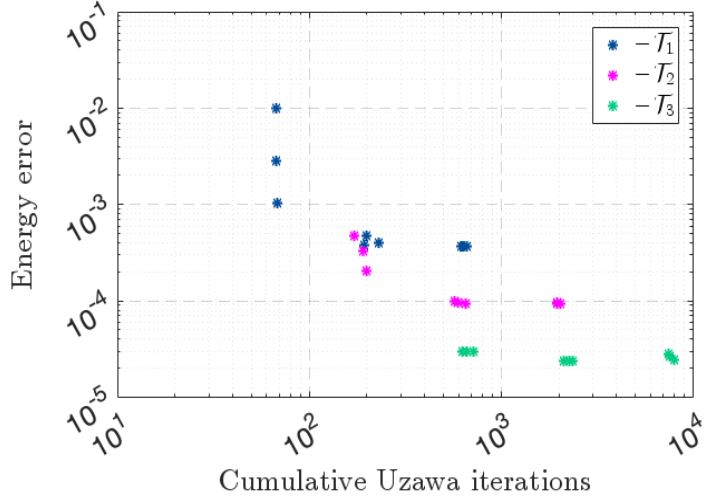


Figure 2: Final energy error ΔE_i versus cumulative Uzawa/ADMM iterations. Each star correspond to a choice of the parameter values ζ and ρ . The color of the stars reflects the level i of mesh refinement. The tolerance is $\varepsilon_{\text{pri}} = 10^{-7}$ on \mathcal{T}_1 and \mathcal{T}_2 and $\varepsilon_{\text{pri}} = 10^{-8}$ on \mathcal{T}_3 .

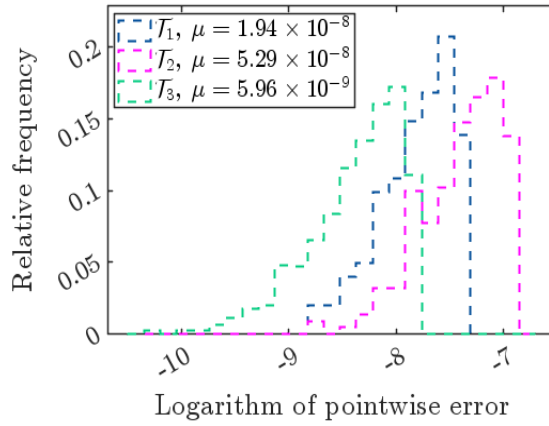


Figure 3: Histograms of absolute pointwise error (logarithm scale) between $p_{\mathcal{T}}^*$ and $\varphi(r_{\mathcal{T}}^*)$ at convergence of outer iteration on the three triangulations. The mean value for each distribution is also reported in the legend.

Figure 3 presents the histograms of the absolute pointwise errors between $p_{\mathcal{T}}^*$ and $\varphi(r_{\mathcal{T}}^*)$ (in logarithmic scale) sampled at each interior mesh vertex for the first three triangulations \mathcal{T}_i , $i \in \{1, 2, 3\}$. The histograms are normalized by the total number of interior mesh vertices. The distributions are supported in the interval $[-8.75, -7.35]$ for $i = 1$, $[-8.77, -6.9]$ for $i = 2$, and $[-10.3, -7.83]$ for $i = 3$. A progressive leftward shift of the mean value (μ), starting from 1.94×10^{-8} on \mathcal{T}_1 to 5.96×10^{-9} on \mathcal{T}_3 , is observed. We also notice that the histogram on \mathcal{T}_2 is slightly worse than that on \mathcal{T}_1 , yet both are compatible with the tolerance set to $\varepsilon_{\text{pri}} = 10^{-6}$.

5.2 Example 2

In this section, we define another analytical solution using the map $\tilde{\Phi} : \mathbb{R}^2 \times \mathbb{R}^2 \rightarrow \mathbb{R}^4$ such that $\tilde{\Phi}(X; \mathbf{x}) = \mathcal{G}(\tilde{\mathbf{n}}^{(3)}(X; \mathbf{x}))$, where $\tilde{\mathbf{n}}^{(3)} := (4\tilde{n}_1^3 - 3\tilde{n}_1, 3\tilde{n}_2 - 4\tilde{n}_2^3)$ for the unit vector $\tilde{\mathbf{n}} = (\tilde{n}_1, \tilde{n}_2)$ described in Example 5.1. The solution presented in Figure 4 is $\Psi_{\mathbf{y}_0}(\mathbf{x}) := \tilde{\Phi}(\mathbf{y}_0, \mathbf{x})$ for all $\mathbf{x} \in \Omega$, with $\mathbf{y}_0 := (1.2, 0.2)^\top$. The four components $\Psi_{\mathbf{y}_0} := (\Psi_1, \Psi_2, \Psi_3, \Psi_4)$ are displayed in Figure 5. The reference exact energy, computed using a sixth-order quadrature on each mesh, is $E(\Psi_{\mathbf{y}_0}) \approx 57.26846$.

This analytical solution is more challenging to approximate than the previous one and motivates the use of one additional level of mesh refinement.

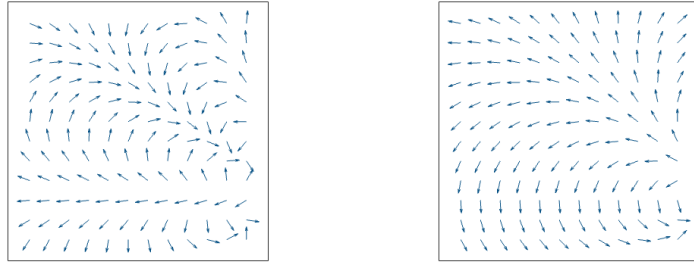


Figure 4: Nematic profile \mathbf{Q} (left) and magnetic profile \mathbf{M} (right) for the exact solution Ψ_{y_0} with $y_0 = (1.2, 0.2)^T$; the domain is $\Omega := (0, 1)^2$.

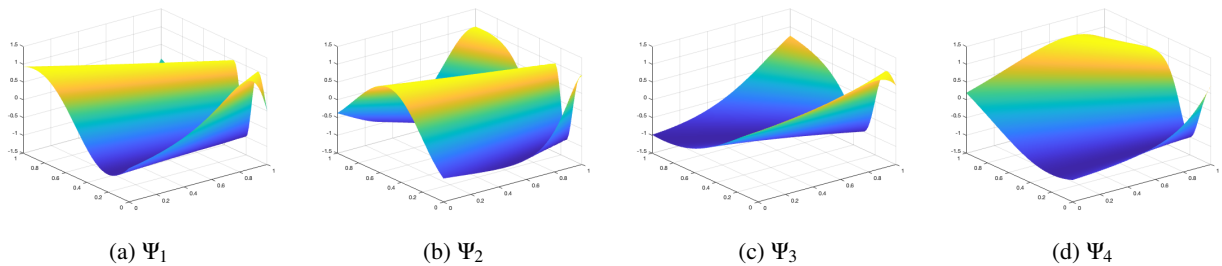


Figure 5: Exact solution $\Psi_{y_0} = (\Psi_1, \Psi_2, \Psi_3, \Psi_4)$.

As detailed in Section 5.1, the choice of the Uzawa/ADMM tolerance ε_{pri} is primarily guided by three criteria: decay of the discrete energy error, energy decrease in the outer loop without oscillation, and computational cost measured by the total number of Uzawa/ADMM iterations. Based on these considerations and repeating the same numerical experiments as above (details are omitted for brevity), we eventually choose $\varepsilon_{\text{pri}} = 10^{-7}$ on \mathcal{T}_1 and \mathcal{T}_2 , $\varepsilon_{\text{pri}} = 10^{-8}$ on \mathcal{T}_3 , and $\varepsilon_{\text{pri}} = 10^{-9}$ on \mathcal{T}_4 , and restrict our analysis to these tolerance values. We notice, in particular, that these choices deliver energy decay at each outer iteration. Table 6 presents the energy error at convergence, $\Delta E_i := E(\Psi_{y_0}) - E(\Psi_{\mathcal{T}_i}^{\text{cv}})$ for the Uzawa/ADMM parameters $\zeta \in \{1, 4, 16\}$, $\rho \in \{1, 0.5, 0.25\}$, and the four triangulations \mathcal{T}_i , $i \in \{1, 2, 3, 4\}$. Compared to Example 5.1, we notice that we have reversed the sign of ΔE_i here as the computed final energy $E(\Psi_{\mathcal{T}_i}^{\text{cv}})$ turns out to be lower than $E(\Psi_{y_0})$. The key observation in Table 6 is the influence of discretization error across meshes. The error ΔE_i is rather substantial on the coarsest mesh and improves significantly under mesh refinement. This indicates the necessity of sufficiently fine triangulations to achieve an accurate approximation of the exact solution, and consequently, of the exact energy. We observe the lowest error ΔE_i for the choice $(\zeta, \rho) = (4, 1)$ if $i = 1$ and $(\zeta, \rho) = (1, 1)$ if $i \in \{2, 3, 4\}$. This observation supports our previous recommendation of choosing a relatively small augmentation parameter ζ on refined meshes. For a fixed ζ , the error can slightly increase as ρ gets smaller.

Next we examine the total number of Uzawa/ADMM iterations for $\zeta \in \{1, 4, 16\}$ and $\rho \in \{1, 0.5, 0.25\}$. Larger values of ζ lead to a higher iteration counts, whereas the influence of ρ is comparatively milder, yielding similar iteration counts in most cases except on \mathcal{T}_1 . On this coarse mesh, the number of iterations increases rapidly with increasing ζ and decreasing ρ . The minimal iteration counts are observed for $(\zeta, \rho) = (4, 1)$ on \mathcal{T}_1 , $(\zeta, \rho) \in \{(1, 1), (1, 0.5)\}$ on \mathcal{T}_2 , $(\zeta, \rho) = (1, 1)$ on \mathcal{T}_3 , and $(\zeta, \rho) = (1, 1)$ on \mathcal{T}_4 . The lowest iteration count is actually observed on \mathcal{T}_2 rather than on \mathcal{T}_1 . Moreover, a similar study to the one reported in Figure 3 on accuracy versus computational cost (figure omitted for brevity) indicates that on every triangulation, the variations in (ζ, ρ) primarily affect the cost rather than the attained accuracy.

$\zeta \setminus \rho$	$\mathcal{T}_1 (\varepsilon_{\text{pri}} = 10^{-7})$			$\mathcal{T}_2 (\varepsilon_{\text{pri}} = 10^{-7})$			$\mathcal{T}_3 (\varepsilon_{\text{pri}} = 10^{-8})$			$\mathcal{T}_4 (\varepsilon_{\text{pri}} = 10^{-9})$		
	1	0.5	0.25	1	0.5	0.25	1	0.5	0.25	1	0.5	0.25
1	5.873	5.885	5.892	1.520	1.521	1.521	0.383	0.384	0.384	0.096	0.096	0.096
4	5.872	5.885	5.892	1.522	1.522	1.522	0.385	0.385	0.385	0.097	0.097	0.097
16	5.872	5.885	5.893	1.522	1.522	1.522	0.385	0.385	0.385	0.097	0.097	0.097

Table 6: Final energy error $\Delta E_i := E(\Psi_{y_0}) - E(\Psi_{\mathcal{T}_i}^{\text{cv}})$ on the four triangulations \mathcal{T}_i , $i \in \{1, 2, 3, 4\}$, and for various choices of the Uzawa/ADMM parameters: $\zeta \in \{1, 4, 16\}$, $\rho \in \{1, 0.5, 0.25\}$, $\varepsilon_{\text{pri}} \in \{10^{-6}, 10^{-7}, 10^{-8}, 10^{-9}\}$.

$\zeta \setminus \rho$	$\mathcal{T}_1 (\varepsilon_{\text{pri}} = 10^{-7})$			$\mathcal{T}_2 (\varepsilon_{\text{pri}} = 10^{-7})$			$\mathcal{T}_3 (\varepsilon_{\text{pri}} = 10^{-8})$			$\mathcal{T}_4 (\varepsilon_{\text{pri}} = 10^{-9})$		
	1	0.5	0.25	1	0.5	0.25	1	0.5	0.25	1	0.5	0.25
1	104	126	193	60	60	65	191	204	217	734	782	853
4	103	158	263	183	195	186	711	738	789	2811	2959	3108
16	185	251	513	631	635	659	2588	2738	2748	9422	10013	10318

Table 7: Total number of Uzawa/ADMM iterations on the three triangulations and for various choices of the Uzawa/ADMM parameters: $\zeta \in \{1, 4, 16\}$, $\rho \in \{1, 0.5, 0.25\}$, $\varepsilon_{\text{pri}} \in \{10^{-6}, 10^{-7}, 10^{-8}, 10^{-9}\}$.

In contrast, mesh refinement leads to an accuracy improvement. Altogether, the results of Tables 6 and 7 suggest the following choices of parameters: $\zeta = 4, \rho = 1, \varepsilon_{\text{pri}} = 10^{-7}$ on \mathcal{T}_1 , $\zeta = 1, \rho = 1, \varepsilon_{\text{pri}} = 10^{-7}$ on \mathcal{T}_2 , $\zeta = 1, \rho = 1, \varepsilon_{\text{pri}} = 10^{-8}$ on \mathcal{T}_3 , and $\zeta = 1, \rho = 1, \varepsilon_{\text{pri}} = 10^{-9}$ on \mathcal{T}_4 .

i	$E(\Psi_{y_0})$	$E(\Psi_{y_0}^I)$	$E(\Psi_{\mathcal{T}_i}^{\text{cv}})$	ΔE_i	rate
1	57.268	51.594	51.396	5.872	–
2	57.268	55.753	55.747	1.522	1.948
3	57.268	56.884	56.886	0.383	1.991
4	57.268	57.172	57.173	0.096	2.001

$j \setminus i$	1	2	3	4
0	-14.90	-36.10	-46.38	-49.78
1	5.872	1.522	0.383	0.096
2	5.872	1.522	0.383	0.096
3	5.872	1.522		
4	5.872	1.522		
5	5.872			
6	5.872			
7	5.872			
8	5.872			
9	5.872			
10	5.872			
11	5.872			
12	5.872			
13	5.872			
14	5.872			

Table 8: Left: exact energy, $E(\Psi_{y_0})$, energy for the nodal interpolation of the exact solution, $E(\Psi_{y_0}^I)$, and computed energy $E(\Psi_{\mathcal{T}_i}^{\text{cv}})$ at convergence, together with the error $\Delta E_i := E(\Psi_{\mathcal{T}_i}^{\text{cv}}) - E(\Psi_{y_0})$ and convergence rates, for the four triangulations \mathcal{T}_i , $i \in \{1, 2, 3, 4\}$. Right: Energy error $\Delta E_i^j := E(\Psi_{\mathcal{T}_i}^j) - E(\Psi_{y_0})$ for the outer iteration index $j \in \{0, 1, \dots\}$ and the mesh index $i \in \{1, 2, 3, 4\}$.

Table 8 (left) reports the energies for the exact solution, Ψ_{y_0} , its nodal interpolation, $\Psi_{y_0}^I$, and the discrete solution $\Psi_{\mathcal{T}_i}^{\text{cv}}$ computed for the above parameters and tolerances. The convergence rate of the corresponding energy error ΔE_i is 2. The energy of the nodal interpolant, $E(\Psi_{y_0}^I)$, turns out to be smaller (even on the finest mesh) than the exact energy. The discrete energy $E(\Psi_{\mathcal{T}_i}^{\text{cv}})$, instead, turns out to be an upper bound on $E(\Psi_{y_0}^I)$, but still stays below $E(\Psi_{y_0})$. However, the final energy error ΔE_i swiftly decays as the mesh is refined (with second order). The energy errors $\Delta E_i^j := E(\Psi_{y_0}) - E(\Psi_{\mathcal{T}_i}^j)$ as a function of

i	H^1 -seminorm	rate	L^2 -norm	rate
1	3.70	–	1.08×10^{-1}	–
2	1.88	0.98	2.55×10^{-2}	2.08
3	0.95	0.98	6.87×10^{-3}	1.89
4	0.48	0.99	1.86×10^{-3}	1.89

Table 9: Errors in energy- and L^2 -norm on $\Psi_{\mathcal{T}_i}^{\text{cv}}$ and convergence rates.

the outer iteration index $j \in \{0, 1, 2, \dots\}$ and the mesh index $i \in \{1, 2, 3\}$ are reported in Table 8 (right). The total number of outer iterations is $j = 14$ on \mathcal{T}_1 , $j = 4$ on \mathcal{T}_2 , and $j = 2$ on \mathcal{T}_3 and \mathcal{T}_4 . Table 9 reports the errors on $\Psi_{\mathcal{T}_i}^{\text{cv}}$ evaluated in the H^1 -seminorm and in the L^2 -norm, together with the corresponding convergence rates. First-order convergence is observed in the H^1 -seminorm, as in the previous test case, whereas here second-order convergence is observed in the L^2 -norm. This improved convergence with respect to the previous test case may be attributed to the fact that the errors are larger here.

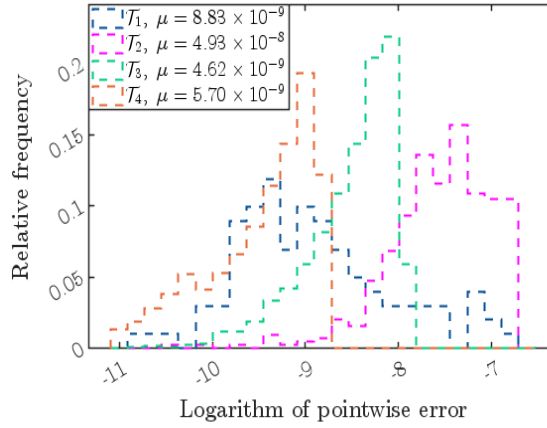


Figure 6: Histograms of absolute pointwise error (logarithm scale) between $p_{\mathcal{T}}^*$ and $\varphi(r_{\mathcal{T}}^*)$ at convergence of outer iteration on the four triangulations. The mean value for each distribution is also reported in the legend.

Finally, the histograms shown in Figure 6 are evaluated from the pointwise errors $\log_{10}(|p_{\mathcal{T}}^* - \varphi(r_{\mathcal{T}}^*)|)$ at each interior mesh vertex for the four triangulations. The error distributions are supported in the interval $[-10.76, -6.83]$ for $i = 1$, $[-10.43, -6.74]$ for $i = 2$, $[-9.73, -7.92]$ for $i = 3$, and $[-11.75, -8.80]$ for $i = 4$. A progressive leftward shift of the histograms is observed, although the behavior is not strictly monotone as the meshes are refined. Altogether, the histograms reflect errors that remain compatible with the prescribed tolerance at each refinement level.

References

- [1] F. Alouges, *A new algorithm for computing liquid crystal stable configurations: the harmonic mapping case*, SIAM J. Numer. Anal. **34** (1997), no. 5, 1708–1726.
- [2] K. J. Arrow, L. Hurwicz, and H. Uzawa, *Studies in linear and non-linear programming*, Stanford Mathematical Studies in the Social Sciences, vol. II, Stanford University Press, Stanford, CA, 1958.
- [3] S. Bartels, *Stability and convergence of finite-element approximation schemes for harmonic maps*, SIAM J. Numer. Anal. **43** (2005), no. 1, 220–238.
- [4] S. Bartels and A. Prohl, *Constraint preserving implicit finite element discretization of harmonic map flow into spheres*, Math. Comp. **76** (2007), no. 260, 1847–1859.

- [5] S. Bartels and A. Raisch, *Simulation of Q -tensor fields with constant orientational order parameter in the theory of uniaxial nematic liquid crystals*, Singular phenomena and scaling in mathematical models, Springer, Cham, 2014, pp. 383–412. MR 3205050
- [6] D. P. Bertsekas, *Constrained optimization and Lagrange multiplier methods*, Computer Science and Applied Mathematics, Academic Press, Inc. [Harcourt Brace Jovanovich, Publishers], New York-London, 1982.
- [7] ———, *Nonlinear programming*, second ed., Athena Scientific Optimization and Computation Series, Athena Scientific, Belmont, MA, 1999.
- [8] F. Bethuel, H. Brezis, and F. Hélein, *Asymptotics for the minimization of a Ginzburg-Landau functional*, Calculus of Variations and Partial Differential Equations **1** (1993), no. 2, 123–148.
- [9] K. Bisht, Y. Wang, V. Banerjee, and A. Majumdar, *Tailored morphologies in two-dimensional ferromagnetic wells*, Phys. Rev. E **101** (2020), 022706.
- [10] J. P. Borthagaray, R. H. Nochetto, and S. W. Walker, *A structure-preserving FEM for the uniaxially constrained Q -tensor model of nematic liquid crystals*, Numer. Math. **145** (2020), no. 4, 837–881.
- [11] J. Brandts, S. Korotov, M. Křížek, and J. Šolc, *On nonobtuse simplicial partitions*, SIAM Rev. **51** (2009), no. 2, 317–335.
- [12] F. Brochard and P. G. de Gennes, *Theory of magnetic suspensions in liquid crystals*, J. Phys. (Paris) **31** (1970), no. 7, 691–708.
- [13] R. Cohen, S. Y. Lin, and M. Luskin, *Relaxation and gradient methods for molecular orientation in liquid crystals*, Comput. Phys. Comm. **53** (1989), no. 1-3, 455–465.
- [14] J. Dalby, P. E. Farrell, A. Majumdar, and J. Xia, *One-dimensional ferromagnetics in a channel: order reconstruction, bifurcations, and multistability*, SIAM J. Appl. Math. **82** (2022), no. 2, 694–719.
- [15] P. G. de Gennes and J. Prost, *The physics of liquid crystals*, 2nd ed., vol. 83, Oxford Science Publication, 1995.
- [16] Q. Du, R. A. Nicolaides, and X. Wu, *Analysis and convergence of a covolume approximation of the Ginzburg-Landau model of superconductivity*, SIAM J. Numer. Anal. **35** (1998), no. 3, 1049–1072.
- [17] M. Fortin and R. Glowinski, *Augmented Lagrangian methods*, Studies in Mathematics and its Applications, vol. 15, North-Holland Publishing Co., Amsterdam, 1983.
- [18] A. J. Hess, Q. Liu, and I. I. Smalyukh, *Optical patterning of magnetic domains and defects in ferromagnetic liquid crystal colloids*, Appl. Phys. Letters **107** (2015), no. 7, 071906.
- [19] S. Y. Lin and M. Luskin, *Relaxation methods for liquid crystal problems*, SIAM J. Numer. Anal. **26** (1989), no. 6, 1310–1324.
- [20] R. R. Maity, A. Majumdar, and N. Nataraj, *Parameter dependent finite element analysis for ferromagnetics solutions*, Comput. Math. Appl. **103** (2021), 127–155.
- [21] A. Mertelj, D. Lisjak, M. Drofenik, and M. Copič, *Ferromagnetism in suspensions of magnetic platelets in liquid crystal*, Nature **504** (2013), no. 7479, 237–241.
- [22] R. H. Nochetto, S. W. Walker, and W. Zhang, *A finite element method for nematic liquid crystals with variable degree of orientation*, SIAM J. Numer. Anal. **55** (2017), no. 3, 1357–1386.
- [23] M. Pierre, *Newton and conjugate gradient for harmonic maps from the disc into the sphere*, ESAIM Control Optim. Calc. Var. **10** (2004), no. 1, 142–167.

- [24] T. Tóth-Katona, P. Salamon, N. Éber, N. Tomašovičová, Z. Mitróová, and P. Kopčanský, *High concentration ferronematics in low magnetic fields*, J. Magn. Magn. Mater. **372** (2014), 117–121.
- [25] J. Xu and L. Zikatanov, *A monotone finite element scheme for convection-diffusion equations*, Math. Comp. **68** (1999), no. 228, 1429–1446.